

**Measuring Colloidal Charges in Low Polar Media from Statistics of
Particle Trajectories**

by

Daniel Jo Evans

A dissertation submitted in partial fulfillment

of the requirements for the degree of

Doctor of Philosophy

Department of Physics

New York University

May 2016

Professor David G. Grier

© Daniel Jo Evans
All Rights Reserved, 2016.

Reason's last step is the recognition that there are an infinite number of things which are beyond it.

— Pascal

Dedication

To my parents

Acknowledgments

I would like to use this opportunity to thank the wonderful people who have made my stay at NYU a rewarding and stimulating experience.

At the top of my list is my advisor, David Grier. Were it not for his brilliance, creativity and generosity, this thesis would not be possible. He is a patient teacher, a kind mentor and an inexhaustible source of inspiration during spells of low productivity despair. His good humor and enthusiasm have infected the whole lab, making for an exciting work environment.

Thanks to the other Grierlings, friends and colleagues who have enriched my life both in and out of the lab. David Ruffner (now at Spheryx) for teaching me about optical tweezers and how to calibrate them. I have yet to see him without a smile on his face. Henrique Moyses is a fountain of joy even in the most stressful of times. I thank him for keeping me down to earth. Thanks to Mark Hannel for listening to my crazy ideas. I thoroughly enjoy all our deep discussions. I also thank Chen Wang, Aaron Yevick and Olawale Jaiyeola, for their unique insights and friendship.

Without the expertise of Andy Hollingsworth, there would be no system to measure at all. Andy has become my unofficial second advisor, not only equipping me with PMMA particles but also with everything I needed to know about nonaqueous colloids. He has taught me more chemistry than I ever could have learned on my own. I deeply admire his knowledge of history and engineering. He is perhaps the most decent person I have ever met.

I would also like to thank William Irvine (now at Chicago) for introducing me to the PMMA-in-CXB system in the first place. Colm Kelleher has been a source of useful

advice. And finally, thanks to friends from my first year graduate cohort who have fought with me in the trenches and have since moved on to bigger and better things: Paul Duffell, James Beacham, Ted Malliaris, Loek van Huysduynen, Krishnaiyengar Karthik, and Lang Feng.

春の花の盛りは、げに、長からぬにしも、おぼえまさるものとなむ。

It is true, as they say, that the blossoms of spring are all the more precious because they bloom so briefly.

Abstract

This thesis presents insights into the mechanism by which colloidal particles can acquire electrostatic charges in apolar media. It introduces advances in experimental techniques for measuring electrostatic interactions between colloidal particles suspended in such media and applies those techniques to a model system. We present precision measurements of the pair interactions between micron-scale poly (methylmethacrylate) (PMMA) spheres dispersed in a fluid medium with a low dielectric constant. Our measurement technique is based on blinking optical tweezer manipulation of dielectric spheres using digital high-speed video microscopy. We extract interaction measurements from particle trajectories using artifact-free particle tracking, making use of optimal statistical methods to reduce measurement errors to the femtonewton frontier while covering an extremely wide range of interaction energies. Despite the absence of charge control agents or added organic salts, these measurements reveal strong and long-ranged electrostatic repulsions consistent with substantial charges on the particles whose interactions are screened by trace concentrations of mobile ions in solution. Electrostatic interactions are revealed to be consistent with the screened-Coulomb potential predicted by DLVO theory. The hydrodynamic interaction is described by low-Reynolds number hydrodynamic coupling for two-spheres in a quiescent fluid. Linear dependence of the estimated charge on particle radius is consistent with charge renormalization theory, and offers insights into the charging mechanism in this interesting class of systems.

Contents

Dedication	iv
Acknowledgments	v
Abstract	vii
List of Figures	x
List of Tables	xii
1 Introduction	1
1.1 Colloids	1
1.2 Historical Overview	4
1.3 Outline of the Work	10
2 Electrostatic Repulsion Between Spheres in a Weak Electrolyte	11
2.1 The Poisson-Boltzmann Equation	11
2.2 DLVO for One Sphere	14
2.3 DLVO for Two Spheres	15
2.4 Charge Renormalization	16
2.5 Summary of Assumptions and Approximations	18
3 Experimental Components	20
3.1 Sample Preparation	22
3.1.1 CXB-dodecane solvent	22
3.1.2 PMMA particles	26

3.1.3	Preparing suspensions	27
3.2	Blinking Optical Tweezers	30
3.2.1	Induced dipole forces on dielectric particles	32
3.2.2	Projecting multiple optical traps: Fourier optics	36
3.2.3	Holographic trapping with spatial light modulators	43
4	Measuring Trajectories of Interacting Particles	45
4.1	Data Acquisition	45
4.2	Image Analysis	48
4.2.1	Centroid detection	48
4.2.2	Particle tracking	53
5	Extracting Forces from Trajectory Data	59
5.1	The Langevin Equation	60
5.1.1	Stokeslet analysis for a single sphere in an unbounded fluid	61
5.1.2	Pair diffusivity	63
5.1.3	Brownian dynamics	66
5.2	Kernel Density Estimation	70
5.2.1	Position and velocity estimates	74
5.3	Diffusivity Estimates	77
5.3.1	Diffusivity profile	78
5.4	Force and Potential Estimates	81
5.5	Charges	86
5.6	Conclusions	89
References		91

List of Figures

1.1	Tyndall Effect	5
1.2	Comparison of double-layer models	8
3.1	Schematic diagram of CXB and dodecane	24
3.2	Scanning electron micrograph of PMMA	26
3.3	PMMA in bulk	28
3.4	Schematic diagram of the optical trapping setup	31
3.5	Two-beam optical trap	34
3.6	Diffraction geometry schematic.	36
3.7	Diffraction with a finite lens	39
3.8	Basic structure of the PAL-SLM.	44
4.1	Hough transformation	49
4.2	Particle detection process	51
4.3	Single-blink trajectory of a pair of $2.3\text{ }\mu\text{m}$ spheres	54
4.4	Midpoint projection method	56
5.1	The Epanechnikov kernel	72
5.2	Sample kernel density estimate compared to histogram	73
5.3	Probability distribution function for positions of $2.3\text{ }\mu\text{m}$ PMMA spheres	75
5.4	Average relative velocity of $2.3\text{ }\mu\text{m}$ PMMA spheres	77
5.5	Average diffusivity of $2.3\text{ }\mu\text{m}$ PMMA spheres	79

5.6	Average interparticle force between 2.3 μm PMMA spheres	82
5.7	Pair potentials $U_{\text{sc}}(r)$ for various sphere sizes	84
5.8	Coulomb and screened-Coulomb fits of pair potentials $U_{\text{sc}}(r)$	85
5.9	Size dependence of effective PMMA charge	87

List of Tables

1.1	Types of colloids	2
3.1	Properties of CXB-dodecane.	22

Chapter 1

Introduction

1.1 Colloids

This thesis focuses on the behavior of colloidal suspensions. Colloids do not constitute a separate type of matter, but represent matter in a particular state of subdivision. They are classified by how one phase of matter is dispersed in another. For example, milk is a suspension of two normally immiscible liquids, oil and water. Table 1.1 lists other types of colloids and their component phases. From this point forward, any mention of colloidal suspensions will refer to **sols**, suspensions of solid particles in a liquid medium, although the techniques outlined here may be adapted for other types of colloids.

The length scales characterizing colloidal systems lie in the regime between the microscopic and the macroscopic, with particles ranging in size from 10 nm to 10 μm . At this length scale, the behavior of colloids depends on a complicated interplay of electrostatic, hydrodynamic, van der Waals, and entropic forces acting upon various composite structures like cells, polymers, and micelles suspended in media that are themselves subject to various forces. Microscopic effects at this scale include ion screening and Brownian motion, which influence the stability of colloidal suspensions against sedimentation and aggregation. Macroscopic effects can be seen in the behavior of large-scale ordered systems created by pair interactions of colloids, as in the case of the visible crystallization of hard sphere suspensions at high volume fraction [1].

Table 1.1: Types of colloids

Type	Dispersed Phase	Continuous Phase	Examples
Liquid aerosol	Liquid	Gas	Mist
Solid aerosol	Solid	Gas	Smoke
Foam	Gas	Liquid	Whipped cream
Emulsion	Liquid	Liquid	Milk
Sol	Solid	Liquid	Paint pigment
Solid Foam	Gas	Solid	Styrofoam
Gel	Liquid	Solid	Gelatin
Solid Sol	Solid	Solid	Opal

One way to distinguish sols is to examine their sensitivity to the introduction of small amounts of electrolyte to the suspending medium [2]. Sols are classified as **lyophobic** if even trace amounts of salt cause the colloidal particles to **flocculate**, or aggregate, ceasing to be suspended in the medium. The additional salt increases the concentration of ions (or **ionic strength**), especially those that screen the particle charge. Electrostatic forces are responsible for keeping colloidal particles separated. Therefore, increased screening suppresses pair electrostatic forces, so that the incessant agitation of the particles' Brownian motion will allow approach within the range of van der Waals attraction, thereby destabilizing the suspension. This process is usually irreversible, even when the salt concentration is subsequently reduced. Gold sols are a good example of lyophobic colloids. Those prepared by Michael Faraday in the 1850s remain suspended today. **Lyophilic** sols such as starch-in-water suspensions tend to be stable, requiring large amounts of electrolyte to aggregate. The flocculation process for lyophilic sols is reversible because affinity of the particles with the medium tends to overpower mutual van der Waals attraction once the ionic strength is lowered. The root “lyo-” of lyophobic and lyophilic derives from the Greek λύω, which means “to loosen, to dissolve.”

A related phenomenon occurs when electrolytes are systematically removed from the

suspension. As the medium becomes deionized, the concentration of available ions to screen colloidal particles decreases, strengthening electrostatic repulsion and inducing a disorder-order transition into a crystalline phase. Polystyrene in deionized water exhibits iridescence due to Bragg diffraction of visible light off the suspended crystallite, which exhibits an order structure formed by the spheres [3]. Colloidal particles must be charged for them to repel each other in this manner. The environments in which these particles are placed tend to be electrically neutral. So how do charges in the medium separate to form a stable colloidal system?

For charge separation (or charge dissociation) to occur, the electric potential energy cannot be much larger than the thermal energy $k_B T = 4.11 \times 10^{-21} \text{ J}$ at room temperature. Thermal energy must be high enough to prevent positive and negative ions from coalescing. The distance of closest approach where thermal fluctuation prevents electrostatic binding between oppositely charged ions with $|q| = e$ is called the **Bjerrum length**,

$$\lambda_B = \frac{1}{4\pi\epsilon\epsilon_0} \frac{e^2}{k_B T}, \quad (1.1)$$

which depends on the relative permittivity of the medium, ϵ . In water, $\epsilon = 79$ at room temperature and the Bjerrum length is 0.7 nm. The scale for thermal separation is comparable to the size of a few water molecules, allowing for molecular-scale solvation of ions [4]. In nonpolar media like dodecane, where $\epsilon = 2$, the Bjerrum length is approximately 30 nm. This makes it energetically unfavorable for ions to separate. If structures can be formed around the ions whose characteristic length is bigger than λ_B , oppositely-charged ions can be separated and like-charged ions can be brought together. These structures are called **inverse micelles** and Hsu *et al.* [5] have found them to regulate charges of colloids in the nonpolar ($\epsilon \lesssim 5$) regime. But a large Bjerrum length does not necessarily preclude

the existence of free ions in low polar solvents when micelles are absent [6, 7].

1.2 Historical Overview

The term **colloid** is derived from the Greek κόλλα meaning “glue,” (many early colloidal studies addressed the properties of glues) and was first coined by Thomas Graham in his 1861 paper “Liquid Diffusion applied to Analysis [8].” In that paper he classified substances based on their ability to diffuse through a thin piece of paper in water. Water soluble solutions of substances like sugar and salt were able to pass though the paper and were termed “crystalloids.” On the other hand, colloids such as albumin, Prussian blue, and gelatin were unable to pass through the paper fibers because their constituent elements were too large. This suggests that colloids are not soluble in their dispersing medium.

Although Graham named them, colloids had been a topic of study since the seventeenth century, when alchemists produced gold sols by treating gold chloride solutions with reducing agents [9, §1.3]. Major advances in colloidal science began in the eighteenth century. Faraday’s lecture on the properties of colloidal gold was delivered four years before Graham published his colloid paper. He discovered that the gold particles in suspension scattered a beam of light so that it became visible to an observer situated at right angles to the beam [10]. This was an early observation of the Tyndall effect, an important development that led to the invention of the ultramicroscope in 1903 by Zsigmondy and Siedentopf [11], and another means to distinguish colloidal suspensions from homogeneous solutions.

Brownian fluctuation is an essential component of the motion of colloids. The botanist Robert Brown in 1827 discovered that tiny particles trapped in water-filled pollen grains of *Clarkia pulchella* would move erratically, although the water was completely still [12].

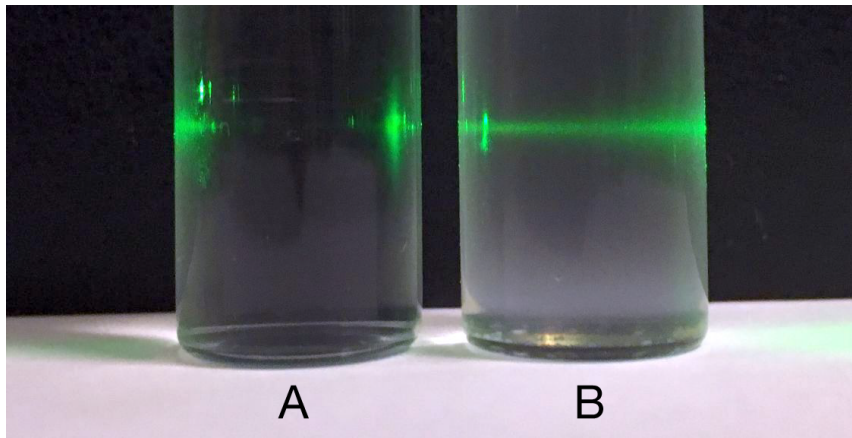


Figure 1.1: Demonstration of the Tyndall effect with a laser. Vial A contains a sugar solution in water, and vial B contains a suspension of $1 \mu\text{m}$ -diameter PMMA spheres in cyclohexyl bromide.

He observed the pollen of many different plants, originally thinking the motion to be a property of life. But observations of the motion of inorganic substances in water revealed the same behavior. Brown called particles undergoing this fluctuation “molecules,” although the actual molecules responsible for Brownian motion were unknown at the time.

No satisfactory explanation for Brownian motion was available until 1909, when Jean Baptiste Perrin experimentally demonstrated the theory of Brownian motion formulated by Albert Einstein [13, 14] and Paul Langevin [15], thereby confirming the atomic theory of matter. In his famous 1905 paper, Einstein developed a diffusion equation for Brownian particles by identifying their motion with the diffusion of solute molecules obeying Maxwell-Boltzmann statistics. He extracted the Stokes-Einstein equation of diffusion by combining van’t Hoff’s laws of osmotic pressure with Stokes law, relating the diffusivity D of a sphere of radius a with the drag force it experiences while moving in a medium with viscosity η :

$$D = \frac{RT}{N_A} \frac{1}{6\pi\eta a}. \quad (1.2)$$

Here, $R = N_A k_B$ is the gas constant and N_A is Avogadro's number. By solving the particle's diffusion equation, Einstein derived another equation bearing his name which relates a Brownian particle's mean-squared displacement to its self-diffusion,

$$\langle x^2 \rangle = 2D\tau = \frac{RT}{N_A} \frac{1}{6\pi\eta a} \tau, \quad (1.3)$$

where τ is the time interval between measurements of a particle's position x . This equation is also an expression for the value of Avogadro's number in terms of measurable quantities, which Perrin confirmed with his experiments [16].

In 1908, Langevin was able to obtain Eq. (1.3) by an independent approach. Instead of using a Fokker-Planck equation to solve for a Brownian particle's probability density, Langevin added a stochastic variable X in Newton's second law to account for fluctuating forces due to molecular bombardment. The equation of motion then becomes

$$m \frac{d^2x}{dt^2} = -6\pi\eta a \frac{dx}{dt} + X. \quad (1.4)$$

Multiplying Eq. (1.4) with x and time-averaging the equation while taking note that $\langle x X \rangle = 0$ and $m \langle (dx/dt)^2 \rangle = RT/N_A$ (from equipartition), Langevin solved Eq. (1.4) for $z = \langle d(x^2)/dt \rangle$, arriving at

$$z = \frac{RT}{N_A} \frac{1}{3\pi\eta a} + C \exp \left[-\frac{6\pi\eta a}{m} t \right]. \quad (1.5)$$

This is equivalent to Eq. (1.3), once we take into account that the exponential term is small for values of t where we observe Brownian motion. We make extensive use of the Langevin equation in Ch. 5, where we derive an expression for the interparticle force

between colloids in terms of their relative velocity and diffusivity.

The charged nature of colloids was known as early as 1809, when Ferdinand Frederic Reuss observed that clay particles in suspension would move in response to a constant electric field. This response is called **electrophoresis**. Reuss also noticed that electrolytes in a capillary would flow under the influence of an electric field, termed **electro-osmosis**. Studies on the flocculation of suspensions with the addition of electrolyte were first made by Schulze in 1882 [17] and Hardy in 1899 [18]. Collectively, these works provided evidence for the electrostatic nature of colloidal stability. Although no theory of screened repulsion or the relation between a particle's charge and electrophoretic mobility existed in the nineteenth century, Hermann von Helmholtz had by 1879 developed a model for the “molecular condenser [19].” This parallel plate capacitor model is another name for the electro-osmotic system, where one plate consists of charges bound to the inner surface of the capillary and the other one is the net charge of free ions in solution. His study of electro-osmosis introduced the concept of the ζ -potential, the electrostatic potential of the charged capillary wall. Marian von Smoluchowski in 1903 was able to relate the ζ -potential of a colloidal particle moving at speed v under the influence of an external electric field E to its electrophoretic mobility [20]

$$\mu_e = \frac{v}{E} = \frac{\varepsilon \varepsilon_0 \zeta}{\eta}. \quad (1.6)$$

This approximate result forms the basic model for electrokinetic phenomena [9, Ch. 7].

It was in the beginning of the twentieth century that Louis Georges Gouy (1910) [21] and later David Chapman (1913) [22] developed a theory for charge screening. Approximating the ionic distribution as a continuous charged ‘cloud,’ they could solve for the potential in Poisson’s equation. In 1923, Debye and Hückel [23] were able to linearize the

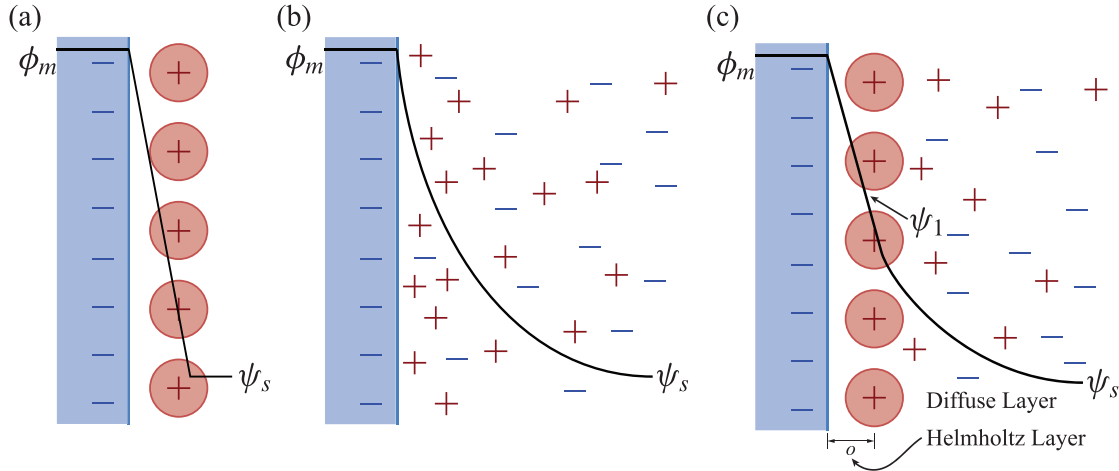


Figure 1.2: (a) The Helmholtz molecular condenser model of the double-layer. (b) The Gouy-Chapman diffuse-cloud model of the double-layer. (c) The Stern model combining the diffuse cloud of Gouy-Chapman and the adsorption of ions to the surface through the Helmholtz model. The quantity ψ_s is the potential of the solution, while ϕ_m is the potential of the surface.

Poisson-Boltzmann equation for the potential of a single ion by assuming it is surrounded by an ionic gas per the Gouy-Chapman model. They related the thickness of the double layer to the ionic strength of the solution. The full theory of colloidal stability with respect to ionic strength was built upon the work of Derjaguin and Landau in 1941 [24] and independently by Verwey and Overbeek in 1948 [2]. It is known as the DLVO theory, combining the ion-ion repulsive screening potential of Debye and Hückel with the pairwise van der Waals attractions calculated by de Boer (1936) and Hamaker (1937). After almost sixty years, the DLVO theory finally explained the observations of Schulze and Hardy, and became the standard model of colloidal interactions.

Little scholarly attention was paid to nonaqueous suspensions until the middle of the twentieth century, when industrial studies began to investigate the nature of charges in dielectric materials. In the electric power industry, the presence of accumulated electrolytes would affect the insulating ability of capacitors [7]. In the petroleum industry, a

large charge buildup in kerosene undergoing a pumping action could result in an explosion, as happened at the Shell refinery in Pernis, Netherlands in 1954 [25]. Klinkenberg and van der Minne found that preferential ion adsorption onto surfaces of trace contaminants would build up large electrostatic streaming potentials with nothing to dissipate excess charges. They showed that the introduction of certain metallic salts like calcium diisopropyl salicylate would increase the conductivity of the fluid and neutralize charge buildup [25, 26].

Developments in emulsion polymerization following the Second World War allowed monodisperse latex particles to be produced for the first time [27]. The 1960s and 1970s brought improved techniques for producing monodisperse polymer spheres [28, 29] stabilized with block and graft co-polymers [30] in nonaqueous suspensions. With these techniques, it became possible construct model systems to experimentally test the DLVO theory in aqueous and nonaqueous systems.

Directly measuring forces between colloids has become possible with the introduction of computer vision hardware and software for tracking individual colloidal particles with adequate temporal and spatial resolution [31, 32]. Some of these techniques build upon the pioneering methods of Perrin [16] by studying the spatial distribution of colloidal particles in equilibrium [33–35]. These techniques yield effective pair potentials in an ensemble-averaged sense [33]. The results gleaned rely on the assumption that many-body distributions can be resolved into pairwise interactions, which may not be justified for some systems [36, 37]. This ambiguity can be lifted by probing the interactions of pairs of particles directly through the introduction of optical trapping techniques [38, 39]. These allow for the manipulation of individual particles, making the measurement of interactions between particles much more convenient [31, 32, 40–43].

1.3 Outline of the Work

The principal aim of this dissertation is to extend the techniques used by Refs. [32, 41] to a nonaqueous apolar ($5 \lesssim \epsilon \lesssim 11$) suspension without the use of dispersants to modify the ionic strength of the medium. Traditionally these dispersants were added to nonpolar ($\epsilon \lesssim 5$) media to provide an environment where ions will be mobile enough to charge particle surfaces. Despite the lack of charge transport structures like inverse micelles, we observe extremely energetic electrostatic particle interactions in our system, on the order of $100 k_B T$ for 1 μm -diameter spheres to $1500 k_B T$ for 5 μm -diameter spheres.

We present a test of the DLVO theory for two charged spheres in a weak electrolyte, exploring the size dependence of particle charge to test the charge renormalization theory explored by Ref. [44]. Chapter 2 outlines the basics of DLVO theory, where we derive the expression for the screened-Coulomb force between two spheres. Chapter 3 provides a description of the experimental components, from the colloidal system to the blinking optical tweezer instrumentation used to perform the measurements. Chapter 4 describes the image detection and processing algorithms designed to track the positions of particles in our measurements. And Chapter 5 derives the principal relation between quantities extracted from particle trajectories to measure the interparticle force and surface charge. It also summarizes the results of our measurements and discusses possible avenues of future study.

Chapter 2

Electrostatic Repulsion Between Spheres in a Weak Electrolyte

To understand the electrostatic interaction of a pair of spheres in a dielectric medium, it is important to investigate the behavior of the electric field in this system. Any real fluid will contain many different species of ions, all undergoing thermal motion and interacting with one another as well as with the charged spheres. Before we place the spheres into solution, we first examine the electric field of the fluid itself by deriving the Poisson-Boltzmann equation (§2.1). In §2.2 we place one charged sphere into the medium and find the electrostatic potential of this arrangement by introducing the Debye-Hückel approximation to the Poisson-Boltzmann equation. Section 2.3 reveals the pair interaction potential between two spheres in this medium. Finally, in §2.4 we briefly explain charge renormalization for colloidal suspensions where sufficiently strong interactions can cause crystallization.

2.1 The Poisson-Boltzmann Equation

Assume the presence of N simple ion species in our medium, each with charge $q_i = e z_i$, where e is the electronic charge and z_i is the valence for the i th species. Then the total free charge density is

$$\rho(\mathbf{r}) = \sum_{i=1}^N q_i n_i(\mathbf{r}) = \sum_{i=1}^N e z_i n_i(\mathbf{r}), \quad (2.1)$$

where $n_i(\mathbf{r})$ is the density of ions of type i , which may have a spatial dependence. The total electrostatic potential $\phi(\mathbf{r})$ satisfies Poisson's equation:

$$\varepsilon \varepsilon_0 \nabla^2 \phi(\mathbf{r}) = -\rho(\mathbf{r}), \quad (2.2)$$

where $\rho(\mathbf{r})$ is the free charge density of all the ions from Eq. (2.1) and ε is the relative permittivity (or dielectric constant) of the medium. At this point we are assuming that $\phi(\mathbf{r})$ is only generated by ions in the fluid. The superposition principle allows us to add the potential generated by charged spheres later. We assume also that this system is in thermal equilibrium, and that ionic concentrations vary slowly on length scales comparable to the inter-ionic separation. Therefore the concentration of the i th species of ions may be treated in the mean-field approximation with the Boltzmann distribution:

$$n_i(\mathbf{r}) = n_i^0 \exp \left[-\frac{e z_i \phi(\mathbf{r})}{k_B T} \right], \quad (2.3)$$

where $k_B T$ is the thermal energy of the solution at temperature T and n_i^0 is the bulk, or mean, concentration of species i . The bulk concentration is the ion concentration far from any sources of interactions, *i.e.* charged interfaces, such that $n_i^0 = \lim_{r \rightarrow \infty} n_i(\mathbf{r})$.

The potentials $\phi(\mathbf{r})$ in Eq. (2.2) and Eq. (2.3) are not actually related. The former is a local potential due to an instantaneous distribution of ions and the latter is a mean-field potential responsible for the ensemble average distribution of ions [9, §4.6]. By equating these potentials, we are applying a mean-field approximation to obtain the **Poisson-Boltzmann equation**,

$$\nabla^2 \phi(\mathbf{r}) = -\frac{e}{\varepsilon \varepsilon_0} \sum_{i=1}^N z_i n_i^0 \exp \left[-\frac{e z_i \phi(\mathbf{r})}{k_B T} \right]. \quad (2.4)$$

The mean-field approximation ignores correlations among the various ion species and any influence of fluctuations. Equation (2.4) and the approximation upon which it is based are the foundations of the Gouy-Chapman model of the ion cloud near a charged surface [21, 22].

Unfortunately, while Eq. (2.4) is a compact equation of state for the diffuse ion cloud, it has no analytic solution, so further simplifications are necessary before we may proceed. We have already assumed that the ions form an ideal gas that satisfies Boltzmann's distribution, where the ions are point charges and the potentials $\phi(\mathbf{r})$ in Eqs. (2.2) and (2.3) are identical. Now if we assume that the electrostatic potential energy for each ion species is small compared to their thermal energy (that is, $e z_i \phi / k_B T \ll 1$), we can linearize the Poisson-Boltzmann equation [2, 23, 24] by Taylor expanding Eq. (2.4), retaining the $\mathcal{O}\{\phi(\mathbf{r})\}$ term:

$$\nabla^2 \phi(\mathbf{r}) = -\frac{e}{\varepsilon \varepsilon_0} \sum_{i=1}^N z_i n_i^0 \left(1 - \frac{e z_i \phi(\mathbf{r})}{k_B T} \right) \quad (2.5a)$$

$$= \frac{e^2}{\varepsilon \varepsilon_0} \sum_{i=0}^N \frac{z_i^2 n_i^0}{k_B T} \phi(\mathbf{r}) \quad (2.5b)$$

$$= \kappa^2 \phi(\mathbf{r}). \quad (2.5c)$$

We eliminate the first term in the right-hand side of Eq. (2.5a) by assuming electroneutrality of the total bulk concentration: $\sum_{i=1}^N e z_i n_i^0 = 0$. The coefficient in front of $\phi(\mathbf{r})$ in Eq. (2.5c) has units of inverse length squared and is related to the **Debye screening length**:

$$\kappa^{-1} = \left(\frac{\sum_{i=1}^N e^2 z_i^2 n_i^0}{\varepsilon \varepsilon_0 k_B T} \right)^{-\frac{1}{2}} = \left(4\pi \lambda_B \sum_{i=1}^N z_i^2 n_i^0 \right)^{-\frac{1}{2}}, \quad (2.6)$$

where λ_B is the Bjerrum length introduced in Eq. (1.1). This quantity provides a length

scale for how ions in solution screen electric fields.

2.2 DLVO for One Sphere

The linearized Poisson-Boltzmann equation can now be solved analytically for some spherical geometries. We first solve it in the presence of one sphere with charge $Q = Ze$ and radius a centered at $r = 0$. The boundary conditions for this case are:

$$(i) \quad \lim_{r \rightarrow \infty} \phi(\mathbf{r}) = 0,$$

$$(ii) \quad \left. \frac{d\phi}{dr} \right|_{r=a} = -\frac{1}{4\pi\epsilon\epsilon_0} \frac{Q}{a^2}.$$

That is, the potential in the bulk becomes negligible due to electroneutrality and the electric field at the surface of the sphere is what we would expect of a charged sphere in a linear dielectric medium. In a spherically symmetric geometry, Eq. (2.5c) becomes

$$\frac{1}{r^2} \frac{\partial}{\partial r} \left(r^2 \frac{\partial \phi}{\partial r} \right) = \kappa^2 \phi(r).$$

Substituting $\psi(r) = r\phi(r)$, we obtain

$$\frac{\partial^2 \psi}{\partial r^2} = \kappa^2 \psi(r),$$

whose general solution is $\psi(r) = Ae^{\kappa r} + Be^{-\kappa r}$. Boundary condition (i) forces $A = 0$ such that $\phi(r) = Be^{-\kappa r}/r$. Solving for B when applying condition (ii) yields

$$B = \frac{Ze}{4\pi\epsilon\epsilon_0} \frac{e^{\kappa a}}{1 + \kappa a}.$$

Thus,

$$\phi(r) = \frac{Ze}{4\pi\epsilon\epsilon_0} \frac{e^{\kappa a}}{1 + \kappa a} \frac{e^{-\kappa r}}{r} \quad (2.7)$$

is the electrostatic potential of a sphere with charge Ze in a dielectric medium with charge carriers. This is equivalent to the screened-Coulomb potential due to a point particle with effective charge number

$$Z^* = Z \frac{e^{\kappa a}}{1 + \kappa a}. \quad (2.8)$$

2.3 DLVO for Two Spheres

Next we superpose the potential of an additional sphere, provided that the ion clouds generated by the spheres do not disrupt each other [45]. Using the effective charge number Z^* from Eq. (2.8) of a sphere in this medium, we may integrate Eq. (2.7) over the surface of another sphere with charge eZ^* at a distance R from the center of the first to obtain the pair potential energy:

$$\begin{aligned} U(R) &= Z^* e \phi(R) \\ &= \frac{(Ze)^2}{4\pi\epsilon\epsilon_0} \frac{e^{2\kappa a}}{(1 + \kappa a)^2} \frac{e^{-\kappa R}}{R} \\ &= k_B T Z^2 \lambda_B \frac{e^{2\kappa a}}{(1 + \kappa a)^2} \frac{e^{-\kappa R}}{R}, \end{aligned} \quad (2.9)$$

where λ_B is the Bjerrum length from Eq. (1.1). Differentiating this result with respect to

R reveals the screened-Coulomb force:

$$\begin{aligned} F(R) &= -\frac{dU}{dR} \\ &= k_B T Z^2 \lambda_B \frac{e^{2\kappa a}}{(1 + \kappa a)^2} \frac{e^{-\kappa R}}{R} \left(\frac{1}{R} + \kappa \right) \\ &= U(R) \left(\frac{1}{R} + \kappa \right). \end{aligned} \quad (2.10)$$

These are the expressions for the electrostatic pair potential and force we will employ going forward. While a complete expression of the DLVO force would require an attractive term, our spheres are no less than 4 μm apart, well beyond the range of appreciable van der Waals forces.

2.4 Charge Renormalization

One of the conditions for Debye-Hückel linearization is that we assume that the potential energy ϕ of each ion species in the medium is small compared to thermal energy scales, or $e z_i \phi / k_B T \ll 1$. This puts a limit on how large surface charges are allowed to be for this linear approximation to be effective. The surface potential ζ of a given sphere is found by evaluating $\phi(r)$ at the surface $r = a$ by using Eq. (2.7) and the definition of the Bjerrum length:

$$\frac{e\zeta}{k_B T} = \frac{e\phi(a)}{k_B T} = \frac{Z\lambda_B}{a(1 + \kappa a)}. \quad (2.11)$$

For $a = 0.5 \mu\text{m}$ and $\lambda_B = 0.7 \text{ nm}$ in deionized water where $\kappa a \ll 1$, Debye-Hückel linearization breaks down at $Z \approx 2000$ [46]. Yet given the large number of binding sites for charges on a given sphere, we would expect the net titratable charge to be much higher.

This does not mean we need to abandon the screened-Coulomb potential that we de-

rived in the previous section. The higher order terms in Eq. (2.4) only increase the screening effect, so that far from the sphere ($r \sim 200\lambda_B$), the Debye-Hückel (DH) potential will look exactly like the exact Poisson-Boltzmann (PB) potential [44, Fig. 2]. This will mean that the Z we extract from the DH potential will be much lower than that of the PB potential. Therefore, provided that we consider regions far from the surface of the sphere and use this lower **renormalized** charge, the DH potential still explains the pair interaction. Henceforward, all charge values and surface potentials will be denoted by their renormalized values Z^* and ζ^* , respectively.

On a further note, the effective charge Z^* of the spheres for $\kappa a < 1$ is limited by a phenomenon called **counterion condensation** [47]. This is a feature of the Poisson-Boltzmann theory and the mechanism by which charge renormalization occurs. Above some critical sphere radius a_c where $Z = -2a_c\lambda_B \ln \kappa a_c$, a thin shell of counterions begins to form near the surface of the sphere, screening out some of the charge. If the sphere radius is comparable to the Debye length κ^{-1} , the sphere appears electrically neutral near its surface. The limiting condition on the effective charge Z^* of the sphere is given by [47, Eq. (3.29)]:

$$Z^* \frac{\lambda_B}{a} < 4 \ln 2 - 2 \ln \kappa a + 2 \ln(-\ln \kappa a) - \frac{1}{2} \ln \left(\frac{Z\lambda_B/a - 2 \ln \kappa a}{Z\lambda_B/a + 2 \ln \kappa a} \right) + \mathcal{O}\{1\}, \quad (2.12)$$

where Z is the sphere's bare charge. We will employ this limit to test how well our measured charges are renormalized in §5.5.

2.5 Summary of Assumptions and Approximations

As we will see in later sections, the DLVO theory works surprisingly well for our system considering the many assumptions we make in setting up and solving the Poisson-Boltzmann equation. Below is a review of approximations especially applicable to our system.

First of all, we assume that our electrolyte consists of point charges suspended in a uniform dielectric medium. This is a valid assumption because the CXB-dodecane mixture we employ contains no complex ion formations with large length scales. The principal charge carriers are hydrogen and bromine ions.

Another assumption we make is a mean-field approximation to equate the potentials in the Poisson equation and the Boltzmann distribution in Eqs. (2.2) and (2.3). As mentioned earlier, the Poisson potential is created by an instantaneous distribution of ions while the Boltzmann potential is formed from an ensemble average of ions in thermal equilibrium. For this to be a valid approximation of an actual system, the ionic concentrations (or ionic strength) should be less than 1 M and the surface potentials on the spheres should be less than 200 mV [9, §4.6]. Conductivity measurements of the CXB-dodecane mixture reveal a low ionic strength, on the order of 10^{-9} M (See §3.1.1 for more information on how we measure the ionic strength of CXB-dodecane). The surface potentials we measure are around $5.1 k_B T/e$, or 130 mV, but the actual potentials may be much bigger, due to nonlinear screening of ions near the particle surface [44]. Screening is sufficiently long-ranged for ion concentration to be low, despite the high surface potential. If we consider the inter-ionic separation described by the Bjerrum length, which is approximately 9.6 nm in a viscous fluid like CXB-dodecane, we may assume ionic concentrations vary slowly

enough so that our mean-field approximation is valid.

The most significant approximation was made in Eq. (2.5a), where we assumed that the electrostatic potential energy of an ion species must be small compared to the thermal energy $k_B T$ for the Poisson-Boltzmann equation to be solvable. This Debye-Hückel approximation is valid so long as we confine our solution to describe the potential energy of a sphere far from its surface, with a renormalized charge Z^* that is much smaller than the actual value Z we would obtain if we were to extrapolate the exact potential back to the surface. One consequence of this approximation is that it works for extremely dilute suspensions, implying that the interaction potential for a collection of spheres may not be pairwise additive [36, 37].

Chapter 3

Experimental Components

We examine a suspension of micron-size **poly(methyl methacrylate)** (PMMA) spheres in a 5:1 mixture (by weight) of **cyclohexyl bromide** (CXB, alternatively bromocyclohexane) and dodecane. The particles contain no fluorescent labeling, and a layer of poly(12-hydroxystearic acid) is covalently attached to their surfaces. While the study of colloids in non-aqueous media stretches back to the 1950s, the study of colloidal interactions and dynamics in density matching fluids is relatively recent. This system was originally developed in 2000 by Eric Weeks, John Crocker, and coworkers who used it to observe hard-sphere colloidal glass transitions of PMMA particles in cycloheptyl bromide (CHB) and decahydronaphthalene (decalin) with confocal microscopy [48]. Like CXB, cycloheptyl bromide is a dense, viscous fluid. When combined with decalin, the mixture produces a density- and index-matching medium for PMMA spheres. Alkyl as well as cycloalkyl halides can react with trace water to produce small amounts of HX (where X represents a halide atom). A halide such as Br is a good leaving group in this regard, and hydrolysis leads to the formation of HBr. Reference [49] employed CXB as an alternative to CHB for its comparative stability. These colloidal systems has the surprising property that the spheres can develop strong and exceptionally long-ranged interactions resembling unscreened Coulomb repulsions. This was very unexpected in a system of electrostatically neutral particles dispersed in a low polar medium. The lower than expected hard-sphere freezing transition was attributed to a long-range electrostatic repulsion imparted by the

fluorophore (a rhodamine salt). However, no charging effects were reported in Ref. [48]. In 2001, de Hoog found that PMMA in CHB-decalin formed face-centered cubic (FCC) crystals with lattice spacing larger than could be explained by particle swelling, indicating a large charge residing on the particles [50, §7.4]. Furthermore, this effect occurred in the absence of rhodamine, ruling out fluorescent dyes as a significant source of particle charge.

Leunissen and coworkers found that carefully cleaning the CXB used to density match the suspension allowed PMMA spheres to form body-centered cubic (BCC) Wigner crystals with extremely large lattice constants, and offered strong evidence that these crystals are stabilized by mutual like-charge repulsion [51]. These crystals' lattice constants, up to $40\text{ }\mu\text{m}$ [52], vastly exceed the micrometer-scale lattice constants that characterize charge-stabilized colloidal crystals in aqueous dispersions, first observed by Kose *et al.* in 1973 [3]. This observation indicates weak screening, which is not surprising given the nominally apolar medium. It also suggests strong charging, which is unexpected because no dispersants or surfactants were added to charge the particles or to modify the screening length of the solvent.

Our study aims to probe the charge state of model colloidal spheres and the nature of their electrolyte environment by measuring the interaction forces between isolated pairs of spheres. Our goals for this set of measurements are to understand the nature of electrostatic interactions in a nominally apolar dispersion and to refine the experimental technique for measuring colloidal interactions. We do this by directly measuring the pair-interaction force that is responsible for this behavior with the use of optical tweezers and digital high-speed video microscopy. In §3.1, we describe how the dispersion is made and characterized. Section 3.2 is an explanation of holographic optical trapping, the central component

Table 3.1: Properties of solvent components. The CXB-dodecane mixture contains 16.7% dodecane by weight. All values measured at 20 °C, except for dielectric constants $\varepsilon_{\text{CXB}} = 7.92$ at 25 °C [53] and $\varepsilon_{\text{dod}} = 2.00$ at 30 °C [54]. The quantities for CXB-dodecane are estimates based on mixture formulas (Eqs. (3.2)–(3.4)).

Solvent	Refractive Index	Density [g/cm ³]	Viscosity [mPa s]
CXB	1.4953 [55]	1.3359 [56]	2.269 [51]
dodecane	1.4212 [57]	0.7488 [57]	1.508 [57]
CXB-dodecane	1.4745	1.181	1.945

of our force probe. The measurements themselves are reported in Chapter 5.

3.1 Sample Preparation

3.1.1 CXB-dodecane solvent

Relevant properties of the solvents used for this study are listed in Table 3.1. Cyclohexyl bromide can decompose to a slight degree into free radicals due to the presence of trace water (hydrolysis). It can also degrade upon exposure to ultraviolet radiation or ultrasound. Through a series of reactions, cyclohexene and hydrogen bromine are produced. The HBr can then dissociate weakly into solvated proton and bromide ions (Fig. 3.1) [58, 59]. This contributes to a relatively weak ionic strength of approximately 10⁻⁹ M. Consequently, this medium is more favorable to ion formation than pure dodecane, but the energy cost for charge separation is still much higher than that of water. The Bjerrum length of CXB is 7 nm compared to dodecane's 30 nm. The nanometer-scale Bjerrum length of CXB limits the concentration of mobile ions, but it does not preclude their existence [6, 60].

As received, CXB (Sigma-Aldrich 135194, ≥ 98% purity) has a measurable conduc-

tivity of approximately 1–8 nS/cm, as measured with a Scientifica Conductivity Meter model 627. At this high conductivity, other products of CXB dissociation such as bromene (Br_2) are visible as a slightly yellow discoloration of the fluid. We purify the CXB by gravity-feeding it through a column of activated alumina and glass wool in a Pasteur pipette to remove polar and acidic molecules such as H_2O and HBr [61]. A syringe filter is used to remove solid fines that may have passed through the glass wool. This activated alumina treatment reduces the conductivity to approximately 50 pS/cm. The conductivity then rises within a few days to a range of 100–150 pS/cm. By adding molecular sieves and storing the purified CXB under nitrogen gas in an opaque glass bottle, we are able to extend the shelf life of our CXB to a few months before another purification cycle is required.

When exposed to trace amounts of water, CXB is known to produce hydrogen bromide through elimination reactions and nucleophilic substitution through a process called **dehydribromination** [62, 63]. This is why, despite our initial filtering and nitrogen padding, some exposure to atmospheric moisture will cause the conductivity of CXB to slowly rise over the course of one year.

To render PMMA spheres neutrally buoyant in the suspension, we mix CXB with 16.7% dodecane by weight. Dodecane is a less-dense nonpolar fluid that serves to match the fluid medium's density with PMMA ($\rho_{\text{PMMA}} = 1.19 \text{ g/cm}^3$, $n_{\text{PMMA}} = 1.492$). Dodecane (Acros Organics 434590010) is a better density matching agent than *cis*-decalin for the purposes of optical trapping in bright-field microscopy because its refractive index is much lower than decalin's ($n_{\text{dec}} = 1.4793$ [57]). This mixture has a refractive index of $n_m = 1.4745$ at optical frequencies, as shown in the third row of Table 3.1, that differs from that of PMMA by enough that we can image the spheres with a conventional bright-field

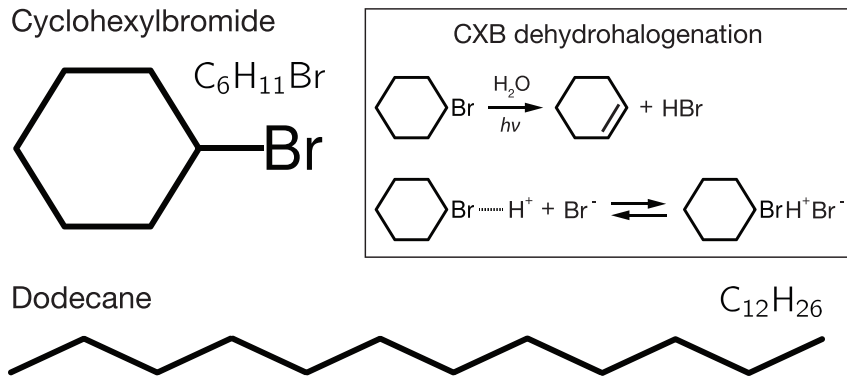


Figure 3.1: Chemical diagrams of CXB and dodecane with simplified formulae for the dissociation of CXB. The presence of Br^- adjusts the relative permittivity of the medium, thereby modulating the degree of HBr dissociation.

microscope without resorting to fluorescent labeling. Although the dodecane lowers the conductivity of the mixture to $\sigma = 26 \text{ pS/cm}$, diminishing the dissociation of pure CXB, care must still be taken not to perturb the mixture with sonication, exposure to ultraviolet light, or excessive heating.

The conductivity of our solvent is related to the concentration n of dissolved ions by the relation $\sigma = \Lambda_0 n$, where Λ_0 is the molar conductance of ions in CXB-dodecane. Assuming that ionic currents are carried solely by HBr, we can estimate Λ_0 from the previously measured value $\Lambda_b = 11.4 \text{ cm}^2 \text{ S mol}^{-1}$, for HBr in 2-butanol ($\epsilon = 16.6$) using the Walden product [64]

$$\Lambda_0 \eta_0 = \Lambda_b \eta_b.$$

Here, $\eta_0 = (1.945 \pm 0.005) \text{ mPa s}$ is the viscosity of CXB-dodecane, as measured by capillary viscometry, and $\eta_b = 3.501 \text{ mPa s}$ is the corresponding value for 2-butanol [65]. From this, we obtain $\Lambda_0 = 20.52 \text{ cm}^2 \text{ S mol}^{-1}$ and a total concentration of monovalent ions of $n = (1.27 \pm 0.05) \times 10^{-9} \text{ M}$. In a conventional electrolyte, dissolved ions contribute to

the Debye-Hückel screening length κ^{-1} , given by Eq. (2.6) and alternatively as

$$\kappa^2 = 4\pi\lambda_B n N_A, \quad (3.1)$$

where N_A is Avogadro's number. Using this formula, we obtain a value of the ionic strength in bulk CXB-dodecane in the absence of spheres, $\kappa_b^{-1} = (3.4 \pm 0.1) \mu\text{m}$. Introducing a water layer to the solvent will cause screening to decrease further as the water acts as a pump that partitions ions out of the oil phase [58, 59]. This may seem counter-intuitive given our explanation of hydrolysis earlier in the section, but ion partitioning is a bulk phenomenon that occurs close to the interface between the oil and water phase.

Finding the density of the CXB-dodecane mixture is straightforward:

$$\rho_m = \rho_{\text{CXB}} v_{\text{CXB}} + \rho_{\text{dod}} v_{\text{dod}}, \quad (3.2)$$

where $v_{\text{CXB}} = 0.74$ and $v_{\text{dod}} = 0.26$ are the volume fractions of CXB and dodecane respectively. To obtain an estimate for the refractive index n_m of the mixture, we apply the Lorentz-Lorenz relation [66]:

$$\frac{n_m^2 - 1}{n_m^2 + 2} = v_{\text{CXB}} \frac{n_{\text{CXB}}^2 - 1}{n_{\text{CXB}}^2 + 2} + v_{\text{dod}} \frac{n_{\text{dod}}^2 - 1}{n_{\text{dod}}^2 + 2}. \quad (3.3)$$

This yields the quoted value of $n_m = 1.4745$. As for finding the dielectric constant of the mixture, Looyenga's formula [67],

$$\varepsilon_m = \left[\left(\varepsilon_{\text{dod}}^{1/3} - \varepsilon_{\text{CXB}}^{1/3} \right) v_{\text{dod}} + \varepsilon_{\text{CXB}}^{1/3} \right]^3, \quad (3.4)$$

yields an estimate of $\varepsilon_m = 5.90$ at low frequencies. However, by measuring the reduced

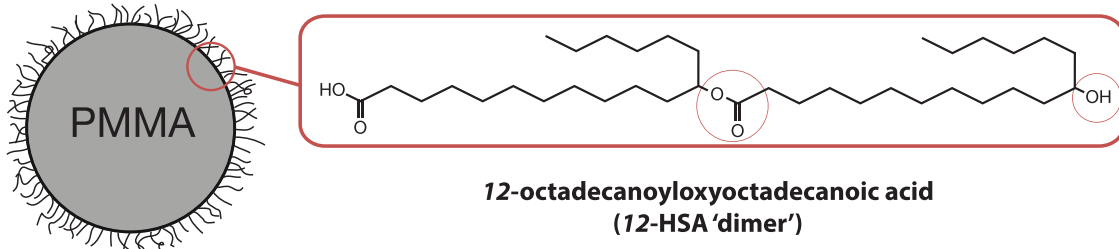
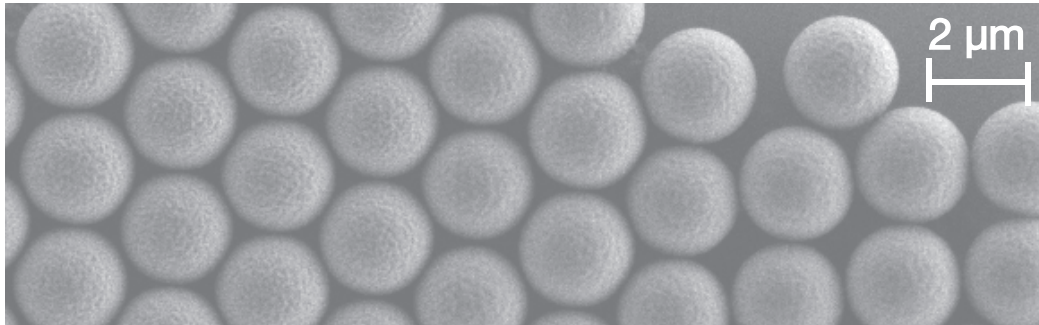


Figure 3.2: (Above) Scanning electron micrograph of 2 μm diameter PMMA spheres functionalized with PHS stabilizer. (Below) Diagram of the steric layer. The PHS component consists of 5-6 monomer units (dimer shown for illustration), with the terminal acid group coupled to a PMMA chain. Circled areas indicate polar regions where charge affinity may occur. Courtesy Andrew Hollingsworth for SEM image.

refractive index of the mixture at various volume fractions of dodecane [51, §2.2.1], we can fit to a nearly linear polynomial that yields a value of $\varepsilon_m = 6.32$.

3.1.2 PMMA particles

The particles in our suspension are monodisperse spheres of poly(methyl methacrylate), produced via dispersion polymerization [29, 68, 69]. They are functionalized with poly(12-hydroxystearic acid) or PHS, a polymer of carbon chains with polar carboxylate groups that form from ester linkages between the polymer components [70]. We functionalize the particles to sterically stabilize them against aggregation. In the absence of dehydrobromination and esterification reactions, such a suspension of uncharged, sterically-stabilized spheres in a density matched medium would behave as a model hard-sphere

system [1, 71, 72].

Following synthesis, the spheres are washed with hexanes to remove unreacted species and then are dried under nitrogen gas before resuspension as a colloid. The monodisperse samples used in this study have particle diameters ranging from 1 μm to 5 μm , with each sample having a polydispersity of 3–5%. Polydispersities were determined by image analysis of scanning electron micrographs of the sort shown in Fig. 3.2.

Using sonication to disperse the particles in the solvent would risk degrading the CXB. We instead vortex the particles first with 0.1 mL of solvent, then with increasing amounts before arriving at the final concentration of spheres.

3.1.3 Preparing suspensions

When suspended in the CXB-dodecane mixture, the nominally neutral PMMA spheres acquire charges and then rapidly deposit onto the glass surfaces of their sample container. This does not happen when the same spheres are dispersed in dodecane alone or in water. Therefore, van der Waals attraction is not likely to explain their deposition. Given that glass carries a slightly negative charge [73], it appears that the PMMA particles develop a positive charge. The presence and sign of the charge is confirmed through electrophoresis in a Malvern Zetasizer Nano ZS equipped with a universal dip cell (ZEN1002) [51, §2.5.1]. Once a monolayer of spheres has deposited on the surface, the effective surface charge presumably changes sign, and the surface is stabilized against further sphere deposition (see Fig. 3.3(a)). The spheres that remain in suspension then become the subjects for our interaction measurements. Neither the solvation of the ions nor the presence of charges on the spheres relies on the addition of charge-stabilizing agents.

One possible origin for the spheres’ positive charge is an ion-dipole association be-

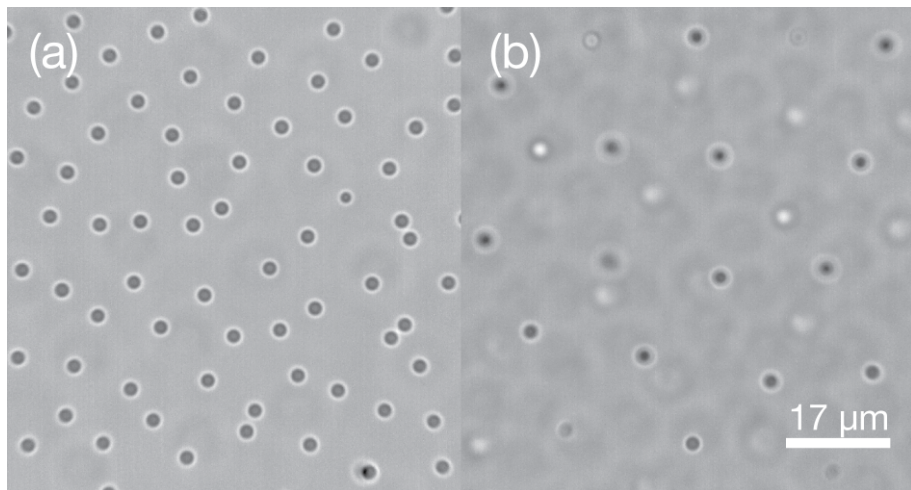


Figure 3.3: (a) Bright-field image of a monolayer of $2.3\text{ }\mu\text{m}$ -diameter PMMA spheres deposited on the surface of the sample cell. (b) A loose Wigner configuration of PMMA spheres in bulk with a volume fraction of $\phi \approx 10^{-2}$.

tween cations in solution and the polar carbonyl groups of the PHS stabilizer layer, including the intended diester linkage between the epoxide-functionalized PHS-g-PMMA stabilizer and surface acid groups. This idea was proposed originally to explain the apparent surface charge behavior of similar colloidal particles suspended in dodecane with added salt [74, 75]. Recently, an alternative mechanism has been proposed [76] in which protons associate with tertiary amine-terminated surface groups resulting from a competing chemical reaction between a catalyst used to couple the stabilizer and the carboxylic acid groups present on the particle surface. The carbonyl groups' dipole moments are four times greater than the amine groups', however [77, 78]. If we account for the entire PHS molecule at an average surface coverage per soluble moiety of 3.5 nm^2 [28] and use 1740 for the average PHS molecular weight [29], we estimate that there are between 10 and 100 more carbonyl groups than amine groups available for proton binding. It is likely that both reactions take place during the so-called stabilizer “locking stage” using dimethylethanolamine. Regardless of the type of dipole at or near the particle surface, the

particle charging mechanism would be same.

Our study requires a low volume fraction of particles so that we can measure pairwise forces with negligible interference from neighboring spheres. However, with too low an initial volume fraction, a large portion of spheres will deposit onto the glass leaving an unrepresentative sample of low-charged spheres suspended in the bulk. Therefore, to achieve sufficient separation of $100\text{ }\mu\text{m}$ or more between neighboring spheres while preventing excessive particle deposition on the walls, we use a mass fraction of PMMA between 0.2% and 0.3%. This corresponds to an initial volume fraction of $\phi_i \approx 10^{-3}$, leading to an effective volume fraction of $\phi_f \approx 10^{-5}$ once the suspension equilibrates. To verify that our suspensions behave similarly to those in earlier reports [58, 59], we also made some samples with higher volume fractions of spheres to observe their original crystal habits. A video micrograph of a typical Wigner crystal at the melting point is shown in Fig. 3.3(b). The appearance of Wigner crystals with lattice constants approaching $20\text{ }\mu\text{m}$ confirms that the suspension is clean of any contaminants that may change the screening length of the solvent and thereby affect the particles' interactions. No more than 50 spheres are immobilized in the field of view. These are few enough and far enough from the focal plane not to interfere with trapping or tracking the pairs of spheres used for interaction measurements.

We find that we can create long-lasting stable samples by sealing our suspensions in $0.1\text{ mm} \times 2.0\text{ mm}$ borosilicate capillary tubes (Vitrocom 5010). Previous implementations of colloidal interaction measurements made use of custom-fabricated sample cells consisting of glass cover slips glued to a microscope slides [32, 42, 79]. Capillary tubes are easier to seal and less likely to get contaminated, and require a less rigorous cleaning regimen than cover slips.

We fill three-quarters of the capillary's length with suspension and one-quarter with deionized water. This is to facilitate preferential absorption of ions from the oil phase into the water phase [59], as explained in §3.1.1. The ends of the tube are sealed and attached to a microscope slide with an ultraviolet curing epoxy (Norland Type 68). To prevent UV decomposition of the solvent, we cover the sample cell with a piece of aluminum foil, except where it makes contact with the epoxy. Some decomposition is inevitable nonetheless. Consistent results obtained from the interaction measurements reported in Ch. 5 suggests that curing for two minutes negligibly affects the screening length of the sample.

Having sealed the cell, we image the suspension with a bright field microscope to check the volume fraction of the sample. Immediately after the sample is prepared, currents arising from equilibration of the ionic species in the oil and water layers may cause particles to drift away from the water layer to fill the rest of the sample. We let this process continue for approximately 30 minutes, until no more drift is evident in the sample. The spheres also swell slightly in this process, increasing their diameter by 3–5% from their dry measurement. This is another reason why we allow the suspension to equilibrate before acquiring data [51, §2.3.2].

3.2 Blinking Optical Tweezers

The primary instrument we use to collect data for measuring colloidal forces is a blinking optical tweezer system [32, 40] attached to a high speed camera [41, 43]. Repeatedly trapping and releasing a pair of spheres and recording their motions while the tweezers are off allows us to reliably build statistics from which to extract the relevant quantities for estimating the pair interaction force [46, §2.3]. A diagram of the setup is presented in

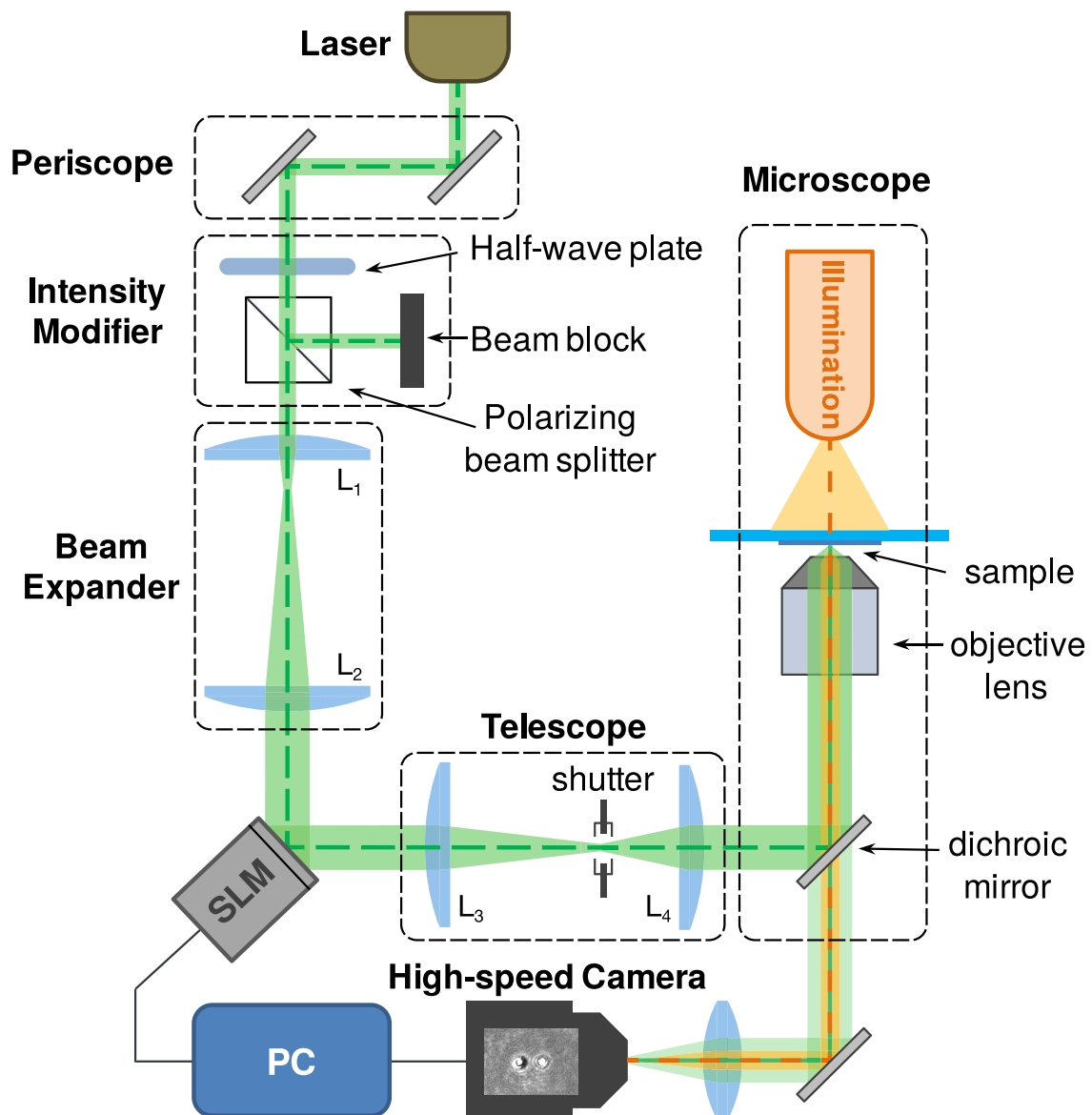


Figure 3.4: Essential components of a high-speed blinking optical trapping setup.

Fig. 3.4.

We project a pair of traps at a vacuum wavelength of 532 nm with a Coherent Verdi V-5 laser beam. A beam expander allows the beam to fill the active area of a liquid crystal spatial light modulator (Hamamatsu PPM X8267), which creates phase patterns that become traps at the focal plane of the microscope's objective lens. The focal lengths of the plano-convex lenses L_1 and L_2 for the expander are 32 mm and 400 mm respectively, corresponding to a magnification of 12.5. To properly fill the back aperture of the objective lens, we use a telescopic setup of two additional plano-convex lenses, labeled L_3 and L_4 , with respective focal lengths 400 mm and 100 mm. We use long-wavelength lenses for the telescope to minimize longitudinal spherical aberrations which may adversely affect trap strength [80].

In §3.2.1, we describe the forces at work in a given optical trap. The Fourier optics of diffraction and refraction are treated in §3.2.2. And in §3.2.3 we explain how a spatial light modulator shapes the phase patterns of an incident beam.

3.2.1 Induced dipole forces on dielectric particles

A simple optical trap works by using tightly a single focused beam of collimated light (usually laser light) to produce a recoil force on a dielectric object of radius a_p directed at the focal point of the beam [38, 81, 82]. If the object is larger than the wavelength λ of the beam (geometrical optics regime), it behaves like a lens that scatters the beam in such a way that the object's recoil conserves linear momentum by moving it towards the focal point [81]. For $a_p \ll \lambda$ (Rayleigh regime), the light induces a dipole moment in the object that experiences forces in the intensity gradient of the beam, that direct the particles to the focus [38]. Forces from the induced dipole moment are still important for objects

comparable to or larger than the beam wavelength ($a_p \geq \lambda$). Here, we explore these dipole forces in more detail.

Let $\mathbf{E}(\mathbf{r}, t)$ be the electric field of the incident beam with angular frequency ω striking a sphere of radius a_p . This electric field is given by

$$\mathbf{E}(\mathbf{r}, t) = \sum_{j=1}^3 u_j(\mathbf{r}) e^{i\varphi_j(\mathbf{r})} e^{-i\omega t} \mathbf{e}_j, \quad (3.5)$$

where \mathbf{e}_j is the j th Cartesian coordinate unit vector. The j th component of the amplitude and phase are $u_j(\mathbf{r})$ and $\varphi_j(\mathbf{r})$ respectively. If the particle is substantially smaller than its wavelength of light in the medium, it develops an induced, oscillating dipole moment at \mathbf{r} :

$$\mathbf{p}(\mathbf{r}, t) = \alpha_e \mathbf{E}(\mathbf{r}, t) \quad (3.6)$$

that is proportional to the electric field at its position \mathbf{r} . In this expression, the polarizability of the object $\alpha_e = \alpha'_e + i\alpha''_e$ is a complex-valued quantity, whose imaginary part accounts for absorption, emission, and radiative losses. Even an ideal dielectric sphere would experience radiative losses when its induced dipole oscillates. These losses are captured in Draine's correction to the Clausius-Mossotti polarizability, given by [83, Eq. (2.6)]

$$\alpha_e = n_m^2 \epsilon_0 \frac{\alpha_e^{(0)}}{1 - \frac{i}{6\pi} k^3 \alpha_e^{(0)}}, \quad (3.7)$$

where $\alpha_e^{(0)}$ comes from the Clausius-Mossotti relation [84, Eq. (2)]

$$\alpha_e^{(0)} = 4\pi a_p^3 \frac{m^2 - 1}{m^2 + 2} \quad (3.8)$$

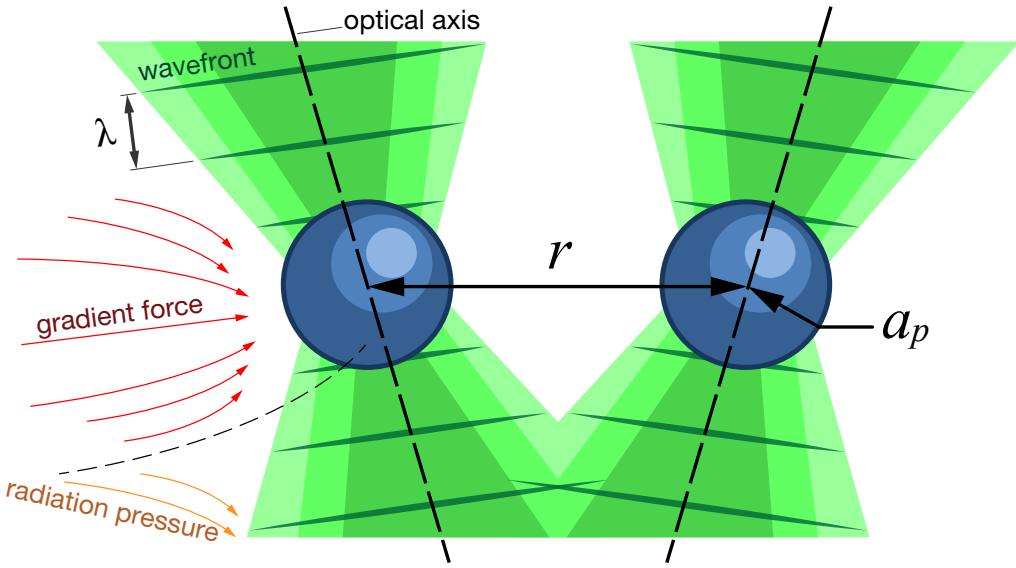


Figure 3.5: A two-tweezer system trapping two spheres of radius a_p displaced a distance r apart. Intense electric field gradients near the focal point of a given trap attract a dielectric sphere towards the center of the trap, overcoming the repulsive force due to radiation pressure. Farther away, radiation pressure dominates and moves the particle along the optical axis.

and $m = n_p/n_m$ is the refractive index ratio of the particle to the medium and ϵ_0 is the vacuum permittivity. The sign of $\alpha_e^{(0)}$ and hence α'_e is positive if the refractive index of the particle is greater than the medium's and negative if $n_m > n_p$. The imaginary part of α_e is always positive and limits the ability of an optical trap to capture an object, as we will see below.

Using the fact that the time-averaged potential energy of an electric dipole is $U = -\Re \{\mathbf{p} \cdot \mathbf{E}\} = -\Re \{\alpha_e\} E^2$, we obtain the gradient dipole force

$$\mathbf{F}_e = -\nabla U = \alpha'_e \nabla E^2. \quad (3.9)$$

The local intensity maximum in a focused beam of light therefore acts as a potential energy well for particles with $\alpha'_e > 0$. Equation (3.9) is not complete however. Oscillation of the

electric field induces a “ponderomotive” force [85] akin to the Lorentz force:

$$\begin{aligned}\mathbf{F}_e &= \nabla \mathbf{p} \cdot \mathbf{E} + \frac{1}{c} \frac{d \mathbf{p}}{dt} \times \mathbf{H} \\ &= \alpha_e \left[\nabla \left(\frac{1}{2} E^2 \right) + \frac{1}{c} \frac{d}{dt} (\mathbf{E} \times \mathbf{H}) \right].\end{aligned}\quad (3.10a)$$

When time-averaged, Eq. (3.10a) becomes [84, Eq. (7)]

$$\langle \mathbf{F}_e(\mathbf{r}) \rangle = \frac{1}{2} \Re \left\{ \alpha_e \sum_{j=1}^3 E_j(\mathbf{r}) \nabla E_j^*(\mathbf{r}) \right\}. \quad (3.10b)$$

Inserting the expression for the electric field in Eq. (3.5) into Eq. (3.10b) yields [86, Eq. (4)]

$$\langle \mathbf{F}_e(\mathbf{r}) \rangle = \frac{1}{4} \alpha'_e \nabla \sum_{j=1}^3 u_j^2(\mathbf{r}) + \frac{1}{2} \alpha''_e \sum_{j=1}^3 u_j^2(\mathbf{r}) \nabla \varphi_j(\mathbf{r}). \quad (3.10c)$$

The first term on the right-hand side of Eq. (3.10c) is an expression for the conservative intensity-gradient force that forms an optical trap (Fig. 3.5). The second term on the right-hand side of Eq. (3.10c) is the non-conservative phase gradient force reported in Ref. [87]. This is more commonly known as the **radiation pressure** or scattering force. An object will mostly absorb rather than scatter optical momentum it is lies far from the focal point of the objective. Beyond a point that depends on α_e , radiation pressure overcomes the gradient force and the object travels down the optical axis of the beam.

If the beam is insufficiently focused due to aberrations caused by a misalignment of the optical train or if a low numerical aperture lens causes the beam to slowly diverge from its focal point, gradient forces will not be strong enough to stably capture objects. Many optical trapping setups incorporate microscope objective lenses, which have high numerical apertures and allow for imaging and trapping objects on the same focal plane

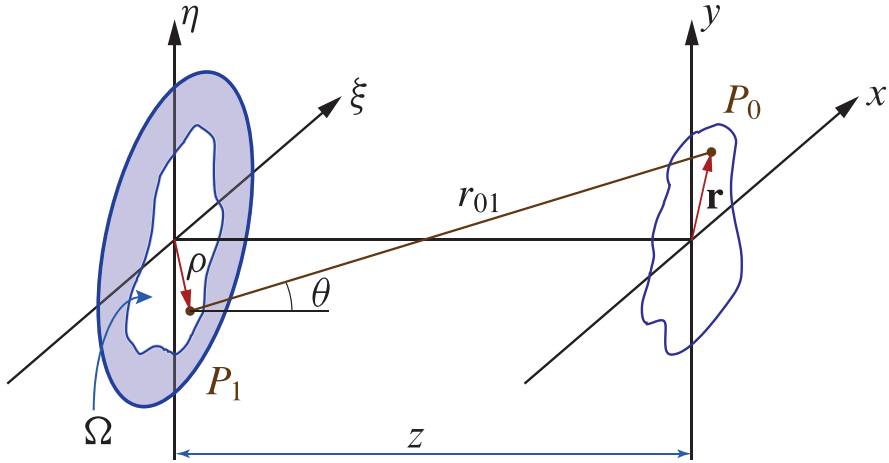


Figure 3.6: Diffraction geometry schematic.

[82]. In our study, we mount samples on a Zeiss Axiovert T100 2TV microscope and image them with 100 \times (for spheres with radii $a_p < 1.5 \mu\text{m}$) and 63 \times (for larger spheres) Zeiss Plan Apo numerical aperture 1.4 oil-immersion lenses.

3.2.2 Projecting multiple optical traps: Fourier optics

Since the discovery of single-beam optical trapping in 1986 [38], advances in optical techniques have facilitated creating and manipulating multiple traps with a single beam of light. One such technique is **holographic optical trapping** (HOT) [39, 80, 88]. A **diffractive optical element** (DOE) in the optical train of the HOT splits the incoming beam into multiple beams before the light enters the telescope in Fig. 3.4. Each of the diffracted beams is directed to the input pupil of the objective lens at an angle chosen to form a trap at the desired position. The DOEs originally used to create multiple optical traps were microfabricated kinoforms [80, 88]. More recent implementations use programmable DOEs known as spatial light modulators (SLMs).

To understand how DOEs work, it may be useful to mathematically describe the principles of Fourier optics relevant to HOTs. A monochromatic plane wave at position P and frequency ω is described by

$$u(P, t) = \Re \{U(P) \exp[-i\omega t]\}, \quad (3.11)$$

where

$$U(P) = A(P) \exp[i\phi(P)] \quad (3.12)$$

is the complex scalar disturbance field containing the phase, ϕ , and amplitude, A , terms. A DOE in the plane of P modifies the amplitude or phase profiles and is represented by the diffraction grating Ω shown in Fig. 3.6. Provided that the size of Ω is much bigger than the wavelength λ of the incident beam, we may discard the vector components of the wave and treat it as a scalar field U [89, §4.1.1] satisfying the Helmholtz equation [90, Eq. (3-13)]

$$(\nabla^2 + k^2) U(P) = 0,$$

where $k = 2\pi/\lambda$ is the wave number of the light. If $P_1 = (\xi, \eta)$ is a point where the incident light hits the grating, we may employ Huygens' principle, which treats each aperture point as a source of diverging spherical waves, to find the scalar field at some point $P_0 = (x, y)$. The diffracted field at P_0 is given by the Rayleigh-Sommerfeld formula [90, Eq. (3-40)]:

$$U(P_0) = \frac{1}{i\lambda} \iint_{\Omega} U(P_1) \frac{\exp[ikr_{01}]}{r_{01}} \cos \theta d\xi d\eta, \quad (3.13)$$

where r_{01} is the scalar displacement between P_0 and P_1 , and θ is the angle between r_{01} and the z -axis, which is normal to the diffraction gradient plane.

Based on the geometry of Fig. 3.6, we may write $\cos \theta = z/r_{01}$, and the distance r_{01} may be expressed in terms of position vectors ρ and \mathbf{r} as

$$r_{01} = \sqrt{z^2 - |\mathbf{r} - \rho|^2}.$$

In the small-diffraction-angle limit, $z \gg |\mathbf{r} - \rho|$, we may approximate r_{01} by

$$r_{01} \approx z \left(1 + \frac{1}{2} \left| \frac{\mathbf{r} - \rho}{z} \right|^2 \right).$$

Applying this result to Eq. (3.13), we obtain the **Fresnel**, or near-field, approximation [90, Eqs. (4-14,17)],

$$\begin{aligned} U(\mathbf{r}) &= \frac{e^{ikz}}{i\lambda z} \iint_{\Omega} U(\rho) \exp \left[i \frac{k}{2z} |\mathbf{r} - \rho|^2 \right] d^2\rho \\ &= \frac{e^{ikz}}{i\lambda z} e^{i \frac{k}{2z} r^2} \iint_{\Omega} \left\{ U(\rho) e^{i \frac{k}{2z} \rho^2} \right\} \exp \left[-i \frac{2\pi}{\lambda z} \mathbf{r} \cdot \rho \right] d^2\rho. \end{aligned} \quad (3.14)$$

We used the fact that $r = \sqrt{x^2 + y^2}$ and $\rho = \sqrt{\xi^2 + \eta^2}$ are the respective magnitudes of the position vectors \mathbf{r} and ρ . Notice that the first line of Eq. (3.14) is a convolution,

$$U(\mathbf{r}) = \iint_{\Omega} U(\rho) h(\mathbf{r} - \rho) d^2\rho, \quad (3.15)$$

where the convolution kernel h is given by

$$h(\mathbf{r}) = \frac{e^{ikz}}{i\lambda z} \exp \left[\frac{ik}{2z} |\mathbf{r}|^2 \right]. \quad (3.16)$$

Aside from the quadratic phase factor outside of the integral, the projected distribution $U(\mathbf{r})$ is simply the Fourier transform of the aperture distribution $U(\rho)$.

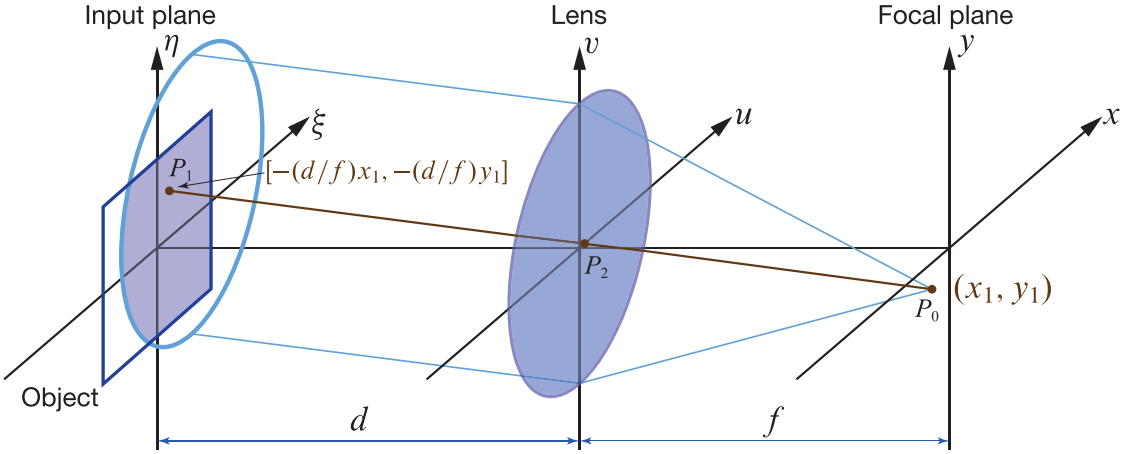


Figure 3.7: Diffraction with a finite lens. The shaded region on the $\xi\eta$ -plane is the portion of the input plane that is transformed by the lens at (x_1, y_1) . Source: [90, Fig. (5.6)]

The objective lens also acts as an agent that transforms the scalar field. This transformation affects the phase of the incoming beam by an exponential factor t_l called the **thickness function**. We obtain this thickness function by noting that a converging lens focuses a beam of light onto a point one focal length away from the uv -plane, as shown in Fig. 3.7. Let r_{02} denote the distance between a point $P_2 = (u, v)$ on the lens and $P_0 = (x, y)$ on the focal plane. Then for a thin lens, the thickness function is given by

$$\begin{aligned}
 t_l(u, v) &\approx \exp[-ikr_{02}] \\
 &= \exp\left[-ik\sqrt{u^2 + v^2 + f^2}\right] \\
 &\approx \exp\left[-i\frac{k}{2f}(u^2 + v^2)\right].
 \end{aligned} \tag{3.17}$$

On the third line of Eq. (3.17), we applied the paraxial approximation, where we assumed that the focal length was much larger than the extent of the lens in the uv -plane.

Now we are ready to combine the results from Eq. (3.14) and Eq. (3.17) to obtain a result for the scalar field that matches our setup shown in Fig. 3.4. The input is the

diffraction grating created by the DOE and the lens is the microscope objective. The telescopic lens pair only serves to relay the field from the DOE to the input plane of the lens, perhaps with magnification. For our purposes its effect may be neglected in our calculation. Figure 3.7 displays this basic setup.

The scalar field in the plane of the lens is

$$U'(u, v) = t_l(u, v) U(u, v),$$

where $U(u, v)$ is the field of the beam leaving the input plane and incident on the lens. The lens applies the thickness function $t_l(u, v)$ to $U(u, v)$, transforming the initial plane wave into a converging spherical wave. The finite extent of the lens must also be taken into account, so we introduce the **pupil function**

$$P(u, v) = \begin{cases} 1 & \text{inside lens aperture} \\ 0 & \text{outside.} \end{cases}$$

The scalar field immediately behind the lens is now

$$\begin{aligned} U'(u, v) &= t_l(u, v) P(u, v) U(u, v) \\ &= P(u, v) U(u, v) \exp \left[-i \frac{k}{2f} (u^2 + v^2) \right]. \end{aligned} \tag{3.18}$$

We are interested in finding the field on the back focal plane, or xy -plane in the geometry we have introduced. Let us first set $d = 0$ so that the input field has no room to propagate before striking the lens. Thus $z = f$ in Eq. (3.14) and after dropping the

constant phase term e^{ikf} , the field on the xy -plane is

$$\begin{aligned} U(x, y) &= \frac{e^{i\frac{k}{2f}(x^2+y^2)}}{i\lambda f} \iint_{\Omega} \left\{ U'(u, v) e^{i\frac{k}{2f}(u^2+v^2)} \right\} e^{-i\frac{2\pi}{\lambda f}(xu+yv)} du dv \\ &= \frac{e^{i\frac{k}{2f}(x^2+y^2)}}{i\lambda f} \iint_{\Omega} U(u, v) \exp \left[-i \frac{2\pi}{\lambda f}(xu+yv) \right] du dv \end{aligned} \quad (3.19)$$

if u and v are within the extent of the lens.

For $d \neq 0$, we need to take a few properties of Fourier transforms into account. We noted that the Fresnel equation effectively describes a Fourier transform of the input field with a quadratic phase term out front. Let $F_0(f_U, f_V) = \mathcal{F}\{U(\xi, \eta)\}$ be the Fourier spectrum of the light transmitted by the input field, and let $F_l(f_U, f_V) = \mathcal{F}\{U(u, v)\}$ be the Fourier spectrum of the light incident on the lens. Based on the second line of Eq. (3.19), $(f_U, f_V) = (u, v)/(\lambda f)$. Assuming that the paraxial approximation holds while the light propagates a distance d from P_1 to P_2 , we use the fact that the Fresnel equation is a convolution (Eq. (3.15)) to obtain

$$\begin{aligned} F_l(f_U, f_V) &= \mathcal{F} \left\{ \iint_{\Omega} U(\xi, \eta) h(u - \xi, v - \eta) d\xi d\eta \right\} \\ &= F_0(f_U, f_V) H(f_U, f_V), \end{aligned}$$

where

$$\begin{aligned} H(f_U, f_V) &= \mathcal{F} \left\{ \frac{e^{ikd}}{i\lambda d} \exp \left[\frac{ik}{2d}(u^2 + v^2) \right] \right\} \\ &= e^{ikd} \exp \left[-i\pi\lambda d (f_U^2 + f_V^2) \right] \end{aligned}$$

is the Fourier transform of the convolution kernel with $z = d$. Ignoring the constant phase term, we obtain

$$F_l(f_U, f_V) = F_0(f_U, f_V) \exp \left[-i\pi\lambda d (f_U^2 + f_V^2) \right]. \quad (3.20)$$

For now, let us assume we are completely within the extent of the lens and set $P = 1$.

Then the field at the focal plane may be written as

$$\begin{aligned} U(x, y) &= \frac{\exp\left[i \frac{k}{2f}(x^2 + y^2)\right]}{i \lambda f} F_l\left(\frac{u}{\lambda f}, \frac{v}{\lambda f}\right) \\ &= \frac{\exp\left[i \frac{k}{2f} \left(1 - \frac{d}{f}\right)(x^2 + y^2)\right]}{i \lambda f} F_0\left(\frac{u}{\lambda f}, \frac{v}{\lambda f}\right) \\ &= \frac{\exp\left[i \frac{k}{2f} \left(1 - \frac{d}{f}\right)(x^2 + y^2)\right]}{i \lambda f} \\ &\quad \times \iint_{\Omega} U(\xi, \eta) \exp\left[-i \frac{2\pi}{\lambda f} (\xi u + \eta v)\right] d\xi d\eta. \end{aligned}$$

Notice further that if $d = f$, the quadratic phase term vanishes, leaving behind an exact Fourier transform. For the purposes of holographic trapping, however, it is desirable to retain some phase curvature to displace optical traps out of the focal plane of the lens.

Taking the finite extent of the lens into account, only a finite set of the rays that end up at a given point (x_1, y_1) could come from the input plane. This set of points is the circular region on the input plane of Fig. 3.7, whose center is the point $(\xi_1, \eta_1) = (-(d/f)u_1, -(d/f)v_1)$, which is created by back-projecting the lens aperture onto the input plane. This process is called **vignetting** [90, §5.2.2]. Applying this process, we find that the center of the pupil function on the $\xi\eta$ -plane is $(-(d/f)u, -(d/f)v)$ and the final

expression for the scalar field at the focal plane becomes [90, Eq. (5-20)]

$$U(x, y) = \frac{\exp\left[i \frac{k}{2f} \left(1 - \frac{d}{f}\right) (x^2 + y^2)\right]}{i \lambda f} \times \iint_{\Omega} U(\xi, \eta) P\left(\xi + \frac{d}{f}u, \eta + \frac{d}{f}v\right) \exp\left[-i \frac{2\pi}{\lambda f} (\xi u + \eta v)\right] d\xi d\eta. \quad (3.21)$$

Vignetting effects are minimized when the input plane is placed against the lens itself ($d = 0$), but for most applications this arrangement is impractical. We may effectively reduce d by using an optical telescope to fill the back aperture of the objective lens, as shown in Fig. 3.4.

3.2.3 Holographic trapping with spatial light modulators

Programmable DOEs for holographic trapping can be created with a computer-addressable **spatial light modulator** (SLM). This device modifies the phase or amplitude of an incoming beam of light to manipulate and project user-defined patterns in real time, so that the output image at the end of the optical train is the array of traps we desire.

The Hamamatsu SLM we use is a PPM (programmable phase modulator), consisting of a PAL-SLM (**P**arallel **A**ligned **L**ematic crystal SLM) coupled to an intensity modulator. A simplified diagram of the PAL-SLM can be found in Fig. 3.8. Amorphous silicon is an optical addressing material that behaves like a photo-conductive layer for the liquid crystal (LC). To enhance the reflecting performance of the SLM, a dielectric material is placed between the LC layer and the silicon. These layers are sandwiched between transparent electrodes, which are further sandwiched between two glass substrate layers. The intensity light modulator (write-in light) creates a computer-controlled phase map that, when displayed onto the amorphous silicon photo-conductor, will cause local

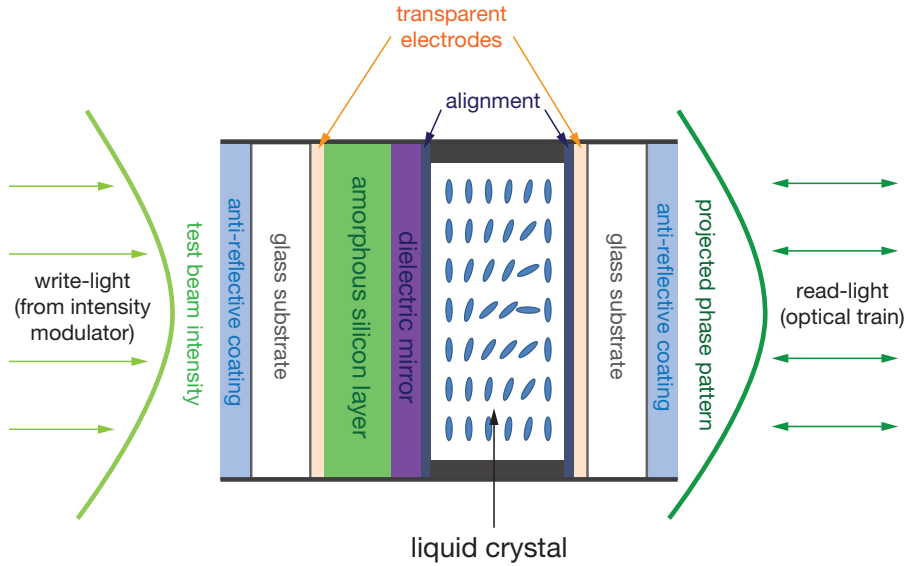


Figure 3.8: Basic structure of the PAL-SLM.

changes to the potential drop between the electrodes. This causes a spatial variation of the refractive index of the LC layer by physically reorienting the crystals. The purpose of this process is to create a phase-modulated wavefront distortion. Phase-modulation is superior to intensity modulation for creating reliable waveforms [91]. This process also mitigates pixel diffraction effects that occur with many LCD SLMs [92].

The active area of our PAL-SLM is $20 \times 20 \text{ mm}^2$ with 768×768 pixels using an X VGA signal format, corresponding to a pixel pitch of $26 \mu\text{m}$. The incident beam strikes the SLM and scatters off with a modified phase that corresponds to the final beam (or set of beams) that we desire. This process may be updated in real time by modifying the phase-pattern sent to the SLM via computer. Holographic diffraction patterns generated by SLMs not only create multiple point traps, but also create optical vortices [93], ring traps [94], line traps [87], solenoid beams [95] and tractor beams [96]. For the purposes of this study however, only dual point traps are employed.

Chapter 4

Measuring Trajectories of Interacting Particles

4.1 Data Acquisition

Blinking optical tweezers allow us to repeatedly position pairs of spheres at set separations to build statistics for accurate interaction estimates. A **blink** is one on-off trapping cycle, implemented with a programmable mechanical shutter (ThorLabs SH05) which lies in the path of the laser beam. The shutter causes mechanical vibrations when it opens and closes, which would disrupt the measurement process if they were permitted to impart lateral forces to the spheres. Care is taken therefore to mechanically isolate the shutter from the rest of the optical trapping setup by attaching it to a massive structure separate from the optical table.

While the traps are on, the spheres are securely fixed in place at the midplane of the sample cell (50 μm from the top and bottom walls of the capillary tube) to minimize sphere-wall interactions. They are also placed at least 50 μm from any nearby particles to avoid spurious sphere-sphere interactions. Stray light from the traps themselves helps in this regard by repelling neighboring spheres with radiation pressure. Traps should remain on for enough time to allow the spheres to return to their starting positions before being released. We operate the laser at 1.5–2 W for effective trapping. This is powerful enough to overcome particle interactions at close separation yet not so powerful as to damage

sensitive equipment such as the SLM.

When the traps are turned off, the particles move freely under the influence of random thermal forces and their mutual interactions. A digital high-speed camera (Fastec HiSpec4 4G Mono) then is triggered to record images at 1500 frames per second using the camera’s maximum possible exposure time (0.6 ms). This ensures sufficient brightness and contrast for image analysis, keeping illumination intensities low enough to avoid sample heating over the course of a 30-minute experiment. The exposure time is short enough to avoid “dynamic error” associated with the motion blurring [97]. As we will explain in further detail in §5.3, this potential source of error is a serious concern for particle-tracking measurements, particularly at small separations where interactions are strong. For 2.3 μm -diameter spheres moving apart at 20 $\mu\text{m}/\text{s}$, dynamic errors cause us to overestimate the spheres’ relative separation by approximately 12 nm.

The timing of each blink is worthy of consideration. If the tweezers are off for too long, particles may wander out of the trapping region and become unrecoverable. It is necessary to use a unique set of particles for each data run, so if a particle is lost, data collected during the current run must be discarded and the gathering process must begin anew. On the other hand, data gathering per blink would be less efficient if we kept the particles trapped for an excessive amount of time. In practice, we extinguish the traps for 100 ms and leave them on for 600 ms in each blink cycle. This ensures that the particles are reliably trapped and released while providing sufficient data per blink in a given data run. We use the camera’s operating software (HiSpec Control with ImageBlitz) to examine the relative brightness of frames, trigger the camera to record when this brightness runs below a threshold indicating that the traps are off, and then record only a set number of frames when the trigger is activated. A 100 ms data collection time at 1500 frames per second

should correspond to 150 frames of trajectory data per blink cycle. However, since the shutter takes a finite amount of time to extinguish the traps, there may be residual light-induced forces acting on the particles after triggering begins. To avoid this, we cut out the first 20 frames, leaving us 130 frames per blink cycle.

A data run consists of sets of trajectory data taken at various initial positions of the traps for two unique spheres. A **set** is a collection of blink data recorded as discrete digital image files for a given initial separation of traps. The recording time for a typical set is 18 real-time seconds. This corresponds to 2.17 seconds of data (25 blink cycles or 3250 frames) for each set. We systematically vary the initial separation of traps to ensure a wide sampling of particle positions, especially when they are more than 5 particle diameters apart, where interactions are much weaker and the spheres move mainly through Brownian motion. Care must be taken when acquiring sets while the traps are 1–2 particle diameters apart, since the interaction is strong enough in this separation regime to move the spheres away from the trapping region too quickly for them to be recaptured. This is why a data run should begin with the traps close together and end with the traps far apart, to reduce the risk of losing one or both spheres during data collection.

At the end of each set, the camera buffer is copied to a computer hard drive for analysis. The images are 400×200 px with a pixel density of 68.5 nm/px when imaging with the $100\times$ objective and 103 nm/px when imaging with the $63\times$ objective. This corresponds to a viewing area of $27.4 \times 13.7 \mu\text{m}^2$ with the $100\times$ objective and $41.2 \times 20.6 \mu\text{m}^2$ with the $63\times$ objective. We choose this viewing area size to capture as wide a range of particle interactions as possible while minimizing data transfer time between sets. At the end of the run, a 2000-frame sequence of background images of the same image size is captured when the spheres depart the viewing area. The purpose of these background images is

explained in §4.2.1.

4.2 Image Analysis

Section 4.1 described the data gathering process. Now we explain how the particles in the image are detected and tracked to create the trajectories required for force measurements.

4.2.1 Centroid detection

The in-plane positions of the spheres are determined to within 10 nm using methods of digital video microscopy implemented by software packages written in the IDL programming environment [98]. Noise and contrast gradients are unavoidable complications that distort a given image, potentially altering the apparent positions of the spheres. We can mitigate some of these effects by using an average compiled from images taken without spheres to correct the background of individual image files. Correcting the background involves dividing the brightness value of each pixel in the image by the corresponding pixel in the background average. While this method was originally developed for analyzing holograms of micrometer-sized colloidal particles [99], background normalization is also effective for cleaning up the bright field images in our study.

One method for quickly detecting circular objects in digital images is a modified circular **Hough transform** with fast convolution methods to pick out particle centers [101, 102]. A Hough transform assigns to each pixel in an image a set of possible descriptors that might describe a curve passing through that pixel. In the classic linear Hough transform, these descriptors are the slope and intercept of lines passing through that point.

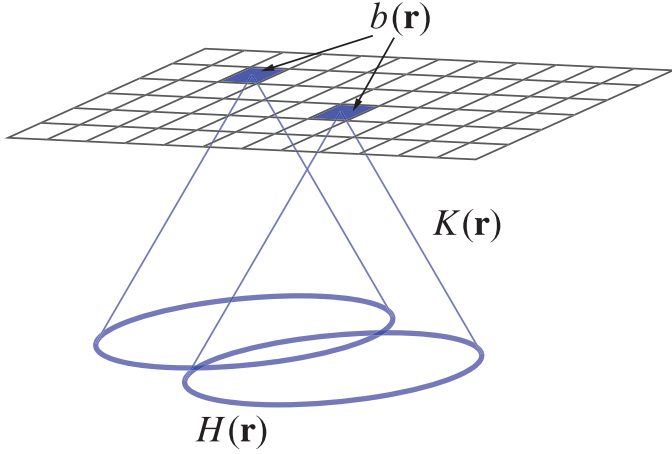


Figure 4.1: Hough transformation $H(\mathbf{r})$ of two image pixels. In reality, $H(\mathbf{r})$ has the same scale of discretization as the input image. Source: Ref. [100, Fig. 1].

In the circular Hough transform they consist of centroids and radii of circles. The weight assigned to each set of descriptors can be determined by non-local estimators of image characteristics such as the local gradient of the brightness. Each pixel in the original image therefore casts votes for possible descriptor values based on these non-local weightings. Votes typically are tallied in accumulator arrays, with peaks corresponding to popular sets of values. These peaks therefore describe features in the original image such as lines and edges for circles and rays.

Each pixel in an image $b(\mathbf{r})$ is assigned a magnitude and direction indicating the degree and orientation of a change in the intensity level at that point [101]. The circular Hough transform replaces a pixel at \mathbf{r} in $b(\mathbf{r})$ with a three-dimensional cone $K(\mathbf{r})$ centered at \mathbf{r} with height and radius determined by the local change in intensity. The cone $K(\mathbf{r})$ is an indicator function for a set of votes made by a single pixel. Convolving $K(\mathbf{r})$ with each pixel in $b(\mathbf{r})$ generates the Hough transform $H(\mathbf{r})$ [100], as shown in Fig. 4.1. However, Hough transforms are computationally complex, requiring $\mathcal{O}\{N^4\}$ operations for images with $N \times N$ pixels [101].

The modified Hough transform used in this study takes the direction of the intensity gradient $\nabla b(\mathbf{r})$ into account. For an image $b(\mathbf{r})$ like Fig. 4.2(d), the magnitude of the two-dimensional gradient $|\nabla b(\mathbf{r})|$ is shown in Fig. 4.2(a). For each pixel in this image there is also an associated direction [102, Eq. (1)],

$$\phi(\mathbf{r}) = \tan^{-1} \left(\frac{\partial_y b(\mathbf{r})}{\partial_x b(\mathbf{r})} \right), \quad (4.1)$$

offering information that contributes to where the center of a feature may be located. A voting algorithm takes this information to tally votes for each pixel in a feature as to where the preferred direction of the intensity gradient is pointing. The pixels with the most votes in the transformed image correspond to centroid locations of circular features, like the one shown in Fig. 4.2(c). Then those centers can be detected using standard algorithms to within 10 nm [98, §III.F]. We explain how the transformation is actually performed for locating local maxima below.

We combine the magnitude and orientation of $\nabla b(\mathbf{r})$ with a two-fold orientation order parameter [102, Eq. (2)]

$$\psi(\mathbf{r}) = |\nabla b(\mathbf{r})|^2 e^{2i\phi(\mathbf{r})}. \quad (4.2)$$

The factor of two in the exponential term takes into account the bi-directional nature of gradient orientation. This parameter is weighted by $|\nabla b(\mathbf{r})|^2$ to emphasize orientations with strong gradients. The kernel we use to convolve $\psi(\mathbf{r})$ is a two-fold symmetric function:

$$K(\mathbf{r}) = \frac{1}{r} e^{2i\theta}, \quad (4.3)$$

where θ is a free parameter that makes $K(\mathbf{r} - \mathbf{r}')\psi(\mathbf{r}')$ real-valued along the line $\mathbf{r}' - \mathbf{r}$ pointing toward $\theta = \phi(\mathbf{r}')$. The full orientation alignment transform is written as [102,

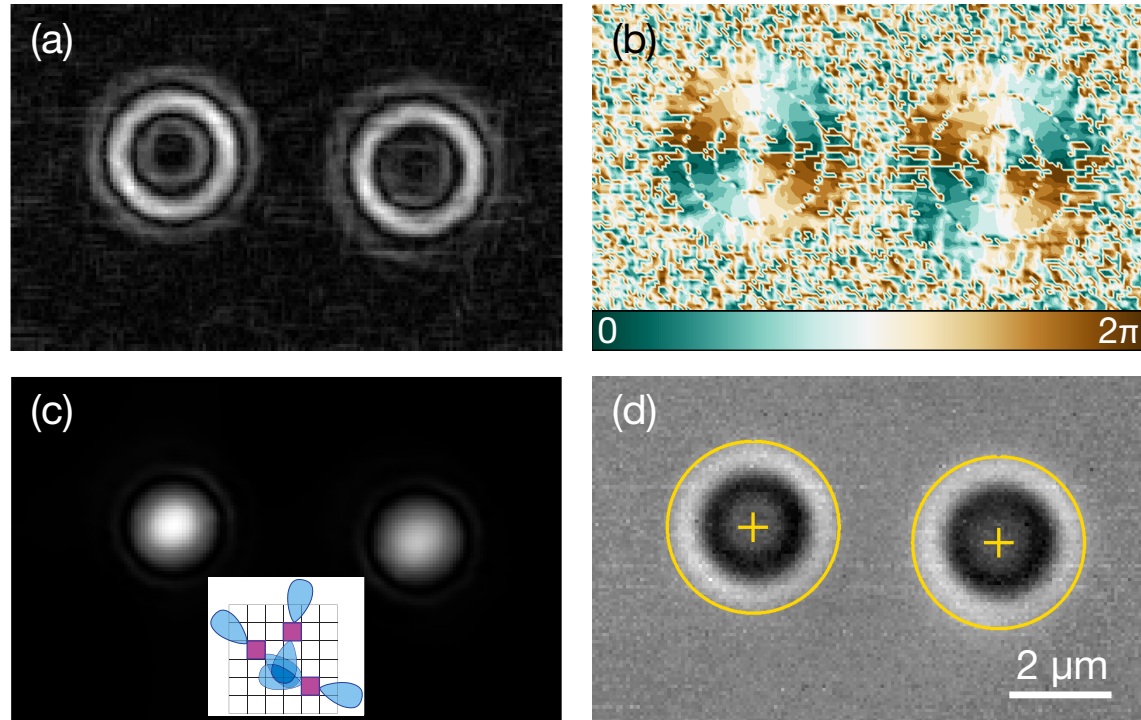


Figure 4.2: Particle detection process from digital images: **(a)** Output of the gradient of intensities of the original image: $|\nabla b(\mathbf{r})|$. **(b)** Orientation of gradients $2\phi(\mathbf{r})$. **(c)** The gradient-weighted orientation-aligned transformed image $B(\mathbf{r})$. Inset: representation of how the real part of $\Psi(\mathbf{r})$ (blue lobes) for three pixels stack to produce $B(\mathbf{r})$. Source: Ref. [102, Fig. 1(d)]. **(d)** Original image $b(\mathbf{r})$ overlaid with circles and crosses marking sphere positions identified by centers of brightness in (c).

Eq. (4)]

$$\Psi(\mathbf{r}) = \int K(\mathbf{r} - \mathbf{r}') \psi(\mathbf{r}') d^2 r'. \quad (4.4)$$

The real parts of $\Psi(\mathbf{r})$ that are oriented in the direction of $\nabla b(\mathbf{r})$ will mostly accumulate at points \mathbf{r} that are symmetry centers in the gradient field. A schematic representation of this process is found in the inset of Fig. 4.2(c). Complex-valued contributions mostly cancel out. Figure 4.2(c) shows that the resultant image $B(\mathbf{r}) = |\Psi(\mathbf{r})|^2$ is a collection of symmetric bright regions whose brightness maxima correspond to particle centers. Figure 4.2(d) confirms this result, with the brightness centers from Fig. 4.2(c) indicated by crosses on the original image.

We can exploit the speed of the **fast Fourier transform** (FFT) to calculate $\Psi(\mathbf{r})$ by transforming the kernel function $K(\mathbf{r})$ and order parameter $\psi(\mathbf{r})$. From the Fourier convolution theorem we can calculate the Fourier transform of $\Psi(\mathbf{r})$ given by

$$\tilde{\Psi}(\mathbf{k}) = \tilde{K}(\mathbf{k}) \tilde{\psi}(\mathbf{k}), \quad (4.5)$$

where $\tilde{\psi}(\mathbf{k})$ is the FFT of $\psi(\mathbf{r})$, and

$$\tilde{K}(\mathbf{k}) = \frac{1}{k} e^{-2i\theta}$$

is the Fourier transform of $K(\mathbf{r})$. Then we apply the inverse FFT on $\tilde{\Psi}(\mathbf{k})$ to obtain the orientation alignment transform described by Eq. (4.4). If we convolve the gradient image $b(\mathbf{r})$ with a Savitzky-Golay smoothing filter [103], we can reduce noise in $b(\mathbf{r})$ while maintaining computational efficiency superior to $\mathcal{O}\{N^3\}$. Overall, the whole process of finding the order parameter $\Psi(\mathbf{r})$ using FFTs requires a total of $\mathcal{O}\{N^2 \log N\}$ operations to complete.

4.2.2 Particle tracking

Having obtained a time-sequenced collection of particle location data grouped in sets of blinks, we next link these up into trajectories. Doing so requires that we determine which particle in a given frame corresponds to one in the preceding frame or set of frames. Many complications arise when making this determination. In the time between successive frames, particles may switch positions, move too close to each other to be reliably distinguished by the software, disappear in one frame and appear in another by moving in and out of focus, or other unforeseen contingencies. We address these concerns with a maximum-likelihood algorithm.

Consider a particle undergoing Brownian motion with self-diffusion coefficient D . The probability that it will move a distance δ in time τ is

$$P(\delta|\tau) = \frac{1}{4\pi D\tau} \exp\left[-\frac{\delta^2}{4D\tau}\right]. \quad (4.6)$$

For an ensemble of N non-interacting particles, with δ_i being the distance the i th particle will move during interval τ , the probability is [98, Eq. (10)]

$$P(\{\delta_i\}|\tau) = \left(\frac{1}{4\pi D\tau}\right)^N \exp\left[-\sum_{i=1}^N \frac{\delta_i^2}{4D\tau}\right]. \quad (4.7)$$

A particle tracking algorithm aims to maximize the probability in Eq. (4.7) while minimizing the mean squared displacement. We refer to identification of features in consecutive frames as a **bond** between those features. For N particles in a given frame, there are $\mathcal{O}(N!)$ possible bonds which suggests that $\mathcal{O}(N!)$ computations of Eq. (4.7) may be required to identify a maximum value for $P(\{\delta_i\}|\tau)$. This is prohibitively expensive com-

putationally even for small values of N .

One method to speed up computation is to assign a maximum length to $\delta = L$ within the time interval τ , assuming a particle moves at an average velocity u such that $u\tau < L$. This parameter L need be only slightly shorter than the typical interparticle separation d . Instead of dealing with a large network of N particles, we can solve for collections of subnetworks contain $M \ll N$ particles. Typically $M = 1$, so the computation time is reduced to $\mathcal{O}\{N \log N\}$ in this trivial case [98, §III.E]. Even when taking interparticle forces into account, the expectation that $\delta < L < d/2$ is reasonable. In our study, spheres are no closer than $d = 4 \mu\text{m}$ apart and move no farther than 20 nm within an inter-frame interval of $\tau = 1/1500 \text{ sec}$. Setting $L \sim 1 \mu\text{m}$ allows for near real-time reliable tracking, even if centroid detection fails for a given particle in one or more frames.

A sample trajectory for a pair of interacting 2.3 μm -diameter spheres in one blink is shown in Fig. 4.3. As this is a two-dimensional trajectory, information on out-of-plane motion is lost. This introduce an unavoidable under-estimation of the force and pair potential [46, §2.5.1] which we can estimate after the fact. When collecting blink data, we are careful to trap the particles on the same focal plane (using the same optics to focus the traps and image the particles) and release them within a small blink interval τ_{blink} to

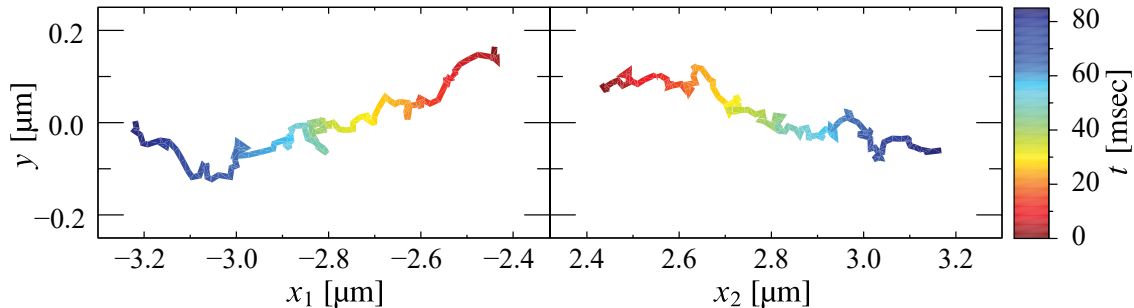


Figure 4.3: Single-blink trajectory of a pair of 2.3 μm -diameter spheres with an initial particle separation of 4.9 μm . The particles move 1.6 μm within the 86 ms blink period.

minimize out-of-plane motion. Generally, out-of-plane motion becomes a concern when the particles are within a couple particle diameters of each other. At this separation, the interparticle force will begin to overpower the intensity gradient force of the traps, moving the particles out of plane slightly even before the traps are extinguished. Increasing the laser power helps to mitigate this effect. Even so, most out-of-plane motion will occur when particles move freely with the traps off.

We can estimate the magnitude of the resulting errors by assuming the out-of-plane angle θ to be small. The in-plane projection r_{2D} of the actual relative separation r_{3D} is $r_{2D} = r_{3D} \cos \theta$. Then the error in separation by accounting for out-of-plane motion is given by

$$\delta = r_{3D} - r_{2D} \approx \frac{\Delta z^2}{r_{2D}}, \quad (4.8)$$

where Δz is the relative out-of-plane displacement of the particles. If we ignore hydrodynamic coupling and only consider the self-diffusion D_0 of each particle, the root-mean-square displacement in the z -direction is given by $\Delta z \approx 2\sqrt{D_0 \tau_{\text{blink}}}$. For 2 μm -diameter spheres at an initial separation of 5 μm , with $\tau_{\text{blink}} = 100 \text{ ms}$ and $D_0 \approx 0.1 \mu\text{m}^2/\text{s}$, the out-of-plane error due to diffusion is $\delta \approx 8 \text{ nm}$, or about 0.2%. This is much lower than for aqueous systems with μm -diameter particles because CXB-dodecane is much more viscous than water and large particles diffuse more slowly than small ones.

Now suppose the particles are moving with a constant in-plane relative velocity u_{2D} due to overdamping of the conservative interparticle force. Suppose further that the force only acts along the axis of particle separation. Then the z -component of this drift velocity is $u_z \approx u_{2D}\theta$. Then $\Delta z = u_z \tau_{\text{blink}} \approx u_{2D}\theta \tau_{\text{blink}}$. For 2 μm -diameter spheres at an initial separation of 5 μm , with $\tau_{\text{blink}} = 100 \text{ ms}$ and a projection velocity of $u_{2D} \approx 20 \mu\text{m}/\text{s}$ at an angle of $\theta \approx 0.2$, the error becomes $\delta \approx 32 \text{ nm}$, or about 0.6%. Together with the error

due to diffusion the total out-of-plane error is approximately 0.8%.

We will need to convert our two-dimensional position data into a one-dimensional form to apply the force relation derived in the following chapter. One way to do this is to simply use the magnitude of the two-dimensional separation vector r_{2D} . This is problematic because even if we discount out-of-plane motion, pairs of particles are more likely to diffuse apart rather than together in two dimensions. This **diffusive drift** may be mistaken as contributing to a repulsive interparticle force [32, 40, 98].

We can eliminate this bias by projecting the dynamics between two consecutive frames of data to one dimension of motion. A recorded data set consists of labeled lists of trajectories $\{\mathbf{x}_1(t_j)\}$ and $\{\mathbf{x}_2(t_j)\}$ for a given blink, measured at times $t_j = j\tau$, where τ is the interval between frames. As shown in Fig. 4.4(a), we can create a discrete set $\{\mathbf{r}_j\}$ of relative displacements corresponding to each frame. Between frames j and $j + 1$, the velocity \mathbf{v}_j is typically defined as

$$\mathbf{v}_j = \frac{\Delta \mathbf{r}_j}{\tau} = \frac{\mathbf{r}_{j+1} - \mathbf{r}_j}{\tau}.$$

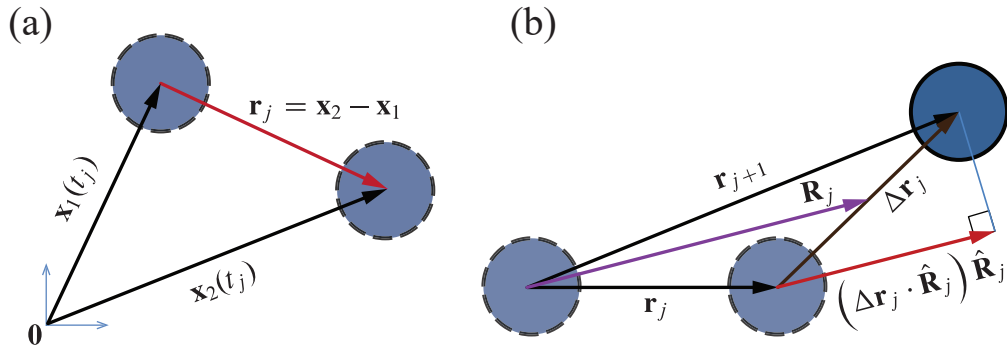


Figure 4.4: Finding a reliable one-dimensional parameter for interparticle separation. **(a)** Standard interparticle separation vector \mathbf{r}_j at time t_j . **(b)** Midpoint interparticle separation vector \mathbf{R}_j (purple arrow) between t_j and t_{j+1} . The midpoint difference vector (red arrow) is parallel to \mathbf{R}_j and determines the one-dimensional velocity instead of $\Delta \mathbf{r}_j$.

However, fictive diffusive drift can manifest itself in components of $\{\mathbf{v}_j\}$ that are normal to the midpoint separation vector,

$$\mathbf{R}_j = \frac{\mathbf{r}_{j+1} + \mathbf{r}_j}{2}. \quad (4.9)$$

To correct for this bias, we project \mathbf{v}_j into the direction of \mathbf{R}_j (see Fig. 4.4(b) for a representative schematic of this projection process) so that the one-dimensional velocity and separation for an arbitrary temporal interval $[t_j, t_{j+n}]$ are

$$v_{j,n}^{\parallel} = \frac{\mathbf{r}_{j+n} - \mathbf{r}_j}{n\tau} \cdot \hat{\mathbf{R}}_{j,n} \text{ and} \quad (4.10a)$$

$$r_{j,n} = \frac{\mathbf{r}_{j+n} + \mathbf{r}_j}{2} \cdot \hat{\mathbf{R}}_{j,n} = R_{j,n}. \quad (4.10b)$$

As we will see in §5.1, this is one of two normal modes in the relative motion frame. The other is motion perpendicular to the axis of separation between the spheres. The velocity in this perpendicular mode is given by

$$\mathbf{v}_{j,n}^{\perp} = \frac{\mathbf{r}_{j+n} - \mathbf{r}_j}{n\tau} - \mathbf{v}_{j,n}^{\parallel}, \quad (4.11)$$

where

$$\mathbf{v}_{j,n}^{\parallel} = \frac{1}{n\tau} \left[(\mathbf{r}_{j+n} - \mathbf{r}_j) \cdot \hat{\mathbf{R}}_{j,n} \right] \hat{\mathbf{R}}_{j,n}$$

defined above. Later in Chapter 5 we will find that $\mathbf{v}_{j,n}^{\perp}$ contributes negligibly to the interparticle force, yet will provide an alternative measurement of the pair diffusivity at infinite separation.

With this one-dimensional information, we are able to consolidate data obtained from multiple blinks at various initial separations over the course of a measurement into a single

data set for analysis. Consolidating one-dimensional data for arbitrary time intervals will be necessary for calculating the average diffusivity in §5.3.

Chapter 5

Extracting Forces from Trajectory Data

Information about particles' interactions is encoded in their trajectories. Before proceeding to extract this information, we need to make certain assumptions about the nature of the forces and their influence on the particles' motions. The **Reynolds number** Re is a good indicator of which inertial regime to consider. This dimensionless quantity, the ratio of inertial forces to viscous forces acting on a sphere in an isotropic fluid medium, is given by [9, §2.2]

$$Re = \frac{\rho UL}{\eta}, \quad (5.1)$$

where U and L are the respective velocity and characteristic length (or diameter) of the sphere, and ρ and η are the respective density and shear viscosity of the fluid. As this is an order of magnitude estimate, the numbers need not be precise. For μm -sized PMMA spheres moving at about $10 \mu\text{m}/\text{s}$, in a medium of CXB-dodecane with $\rho = 1 \text{ g}/\text{cm}^3$ and $\eta = 2 \text{ mPa s}$ (see Table 3.1), the Reynolds number is small: $Re = 10^{-5}$. Therefore viscous forces dominate and the sphere's motion is overdamped.

Motion at low Reynolds number is **Markovian**, or history-independent. This means that trajectory data obtained when particles start out close together and subsequently drift apart are fully compatible with data taken while the particles are initially apart. The Markovian nature of particle interactions in our system allows us to amass an ensemble of

trajectories into a single data set for the purpose of measuring two particles' separation-dependent interactions. The assumption of Markovian dynamics also allows us to analyze the same trajectory data over a range of time intervals and to collect the results into an ensemble average. This is called **greedy sampling** [104]. Section §5.1.2 explains how we exploit greedy sampling to calculate diffusivity estimates.

5.1 The Langevin Equation

A collection of N neutrally buoyant spheres with radius a is suspended in a viscous medium, with the i th sphere at position \mathbf{x}_i . Each sphere experiences an interparticle force $\mathbf{F}(\mathbf{x}_i, \mathbf{x}_j)$ and a thermal noise force $\mathbf{f}_i(t)$. No torques are exerted on any of the spheres. Also, the i th sphere feels a drag force that is proportional to its own velocity and that of the other spheres. In other words, the spheres are **hydrodynamically coupled** to one another. When two particles are hydrodynamically coupled, the fluid motion generated by one sphere influences the motion of the other, whose local fluid motion will affect the first sphere again.

With these components, the general equation of motion or **Langevin equation** [15], for the i th sphere is

$$m \frac{d^2 \mathbf{x}_i}{dt^2} = \sum_{j=1}^N \left(\mathbf{F}(\mathbf{x}_i, \mathbf{x}_j) - b_{ij}^{-1} \frac{d \mathbf{x}_j}{dt} \right) + \mathbf{f}_i(t). \quad (5.2)$$

The quantity b_{ij} in Eq. (5.2) is called the **mobility tensor**. For a single particle, this mobility tensor is simply the inverse of Stokes drag coefficient $\gamma = 6\pi\eta a$, such that when a constant force \mathbf{F}_0 is exerted on a sphere in a medium with viscosity η , the steady-state

velocity \mathbf{v}_0 is

$$\mathbf{v}_0 = \frac{1}{\gamma} \mathbf{F}_0 = b_0 \mathbf{F}_0.$$

More generally, a force $\mathbf{f}(\mathbf{x}_j)$ applied to sphere j creates a flow field $\mathbf{u}(\mathbf{x}_i)$ at the position of sphere i of the form [105, 106]

$$\mathbf{u}(\mathbf{x}_i) = G(\mathbf{x}_i - \mathbf{x}_j) \mathbf{f}(\mathbf{x}_j), \quad (5.3)$$

where $G(\mathbf{x}_i - \mathbf{x}_j)$ is the **Oseen tensor**. This flow field then extends hydrodynamic forces on the i th sphere. In the Stokeslet approximation, the source of the flow is treated as a point excitation, and $G(\mathbf{x}_i - \mathbf{x}_j)$ takes the form of the Green's function for the flow. This Green's function is known as a Stokeslet. The fluid velocity $\mathbf{u}(\mathbf{x})$ satisfies Stokes equations [9, Eq. (2.5.3)]:

$$\begin{aligned} \nabla \mathbf{u} &= 0, \\ \nabla p &= \eta \nabla^2 \mathbf{u} + \delta(\mathbf{x}) \mathbf{f}, \end{aligned}$$

where p is the dynamic pressure and $\delta(\mathbf{x}) \mathbf{f}$ is a point force at the origin. The Stokes equations govern fluid motion at the low Reynolds number regime, and their linearity explains the linearity of Eq. (5.3).

5.1.1 Stokeslet analysis for a single sphere in an unbounded fluid

This flow field will advect a sphere located at \mathbf{x}_i . If the sphere also is acted on by an external force \mathbf{F} , its velocity \mathbf{v}_0 is given by **Faxén's first law** [9, Eq. (2.6.4)]:

$$\mathbf{v}_0 = -b_0 \mathbf{F} + \mathbf{u}(\mathbf{x}) + \frac{1}{6} a^2 \nabla^2 \mathbf{u}(\mathbf{x}). \quad (5.4)$$

In this far-field approximation we see that if the fluid is quiescent, $\mathbf{u}(\mathbf{x}) = \mathbf{0}$ and

$$\mathbf{F} = -\frac{1}{b_0}\mathbf{v}_0 = -6\pi\eta a\mathbf{v}_0,$$

which indicates that the net force on the sphere moving at velocity \mathbf{v}_0 is just the Stokes drag force. Conversely, if no external forces act on the sphere, $\mathbf{F} = \mathbf{0}$ and the sphere is advected by the external flow field.

In general, we may describe the flow field $\mathbf{u}(\mathbf{x})$ created by a sphere of radius a moving with constant velocity \mathbf{v} with the use of Stokeslets [105, §7.3]. The Oseen tensor (or Stokeslet) is the Green's function of the flow field generated by a point source at \mathbf{x}_0 , taking the form

$$G(\mathbf{x}, \mathbf{x}_0) = \frac{1}{8\pi\eta x} \left(\mathbf{I} + \frac{(\mathbf{x} - \mathbf{x}_0)(\mathbf{x} - \mathbf{x}_0)}{x^2} \right), \quad (5.5)$$

where \mathbf{I} is the unit tensor. The \mathbf{xx} term is the outer product or **dyadic** of \mathbf{x} and $x = |\mathbf{x} - \mathbf{x}_0|$.

In component form, with coordinates $\alpha, \beta = 1, 2, 3$, Eq. (5.5) is written as

$$G^{\alpha\beta}(\mathbf{x}, \mathbf{x}_0) = \frac{1}{8\pi\eta x} \left(\delta^{\alpha\beta} + \frac{(x^\alpha - x_0^\alpha)(x^\beta - x_0^\beta)}{x^2} \right). \quad (5.6)$$

The second-order Stokeslet H is called a **stresslet** [9, §2.5] or **potential dipole** [105, §7.2] and is given by

$$H(\mathbf{x}, \mathbf{x}_0) = \frac{1}{8\pi\eta x^3} \left(-\mathbf{I} + 3 \frac{(\mathbf{x} - \mathbf{x}_0)(\mathbf{x} - \mathbf{x}_0)}{x^2} \right), \quad (5.7)$$

also generated by the sphere. The generalized flow field is written as a linear combination

of the Stokeslet and stresslet [105, Eq. (7.3.4)]:

$$\mathbf{u}(\mathbf{x}) = G(\mathbf{x}, \mathbf{x}_0)\mathbf{m} + H(\mathbf{x}, \mathbf{x}_0)\mathbf{n},$$

where \mathbf{m} and \mathbf{n} are vector coefficients for G and H respectively. Without loss of generality, we may set $\mathbf{x}_0 = \mathbf{0}$. Applying the boundary condition $\mathbf{u} = \mathbf{v}_0$ at $x = a$ yields the following equations

$$\begin{aligned} 8\pi\eta a^3 \mathbf{v}_0 &= \mathbf{m}a^2 - \mathbf{n} && \text{for } i = j, \\ \mathbf{0} &= \mathbf{m}a^2 + 3\mathbf{n} && \text{for } i \neq j. \end{aligned}$$

Thus we obtain

$$\mathbf{m} = 6\pi\eta a \mathbf{v}_0 \quad \mathbf{n} = -2\pi\eta a^3 \mathbf{v}_0$$

such that the final expression for $\mathbf{u}(\mathbf{x})$ in terms of \mathbf{v}_0 is [107, Eq. (4.6)]

$$\begin{aligned} \mathbf{u}(\mathbf{x}) &= \mathbf{v}_0 \cdot \left[\frac{3}{4} \frac{a}{x} \left(\mathbf{I} + \frac{\mathbf{xx}}{x^2} \right) + \frac{1}{4} \frac{a^3}{x^3} \left(\mathbf{I} - 3 \frac{\mathbf{xx}}{x^2} \right) \right] \\ &= \mathbf{v}_0 \cdot \left[\mathbf{I} \left(\frac{3a}{4x} + \frac{a^3}{4x^3} \right) + \frac{\mathbf{xx}}{x^2} \left(\frac{3a}{4x} - \frac{3a^3}{4x^3} \right) \right]. \end{aligned} \tag{5.8}$$

We can reproduce the result of Eq. (5.8) to first order in x by assuming that G is solely responsible for the flow field generated by the sphere.

5.1.2 Pair diffusivity

We next consider the hydrodynamic coupling between two spheres of radius a with center-to-center separation $\mathbf{r} = \mathbf{x}_2 - \mathbf{x}_1$. If $r \gg a$, we may ignore lubrication forces and

treat each sphere as moving in the flow field \mathbf{G} generated by the other. We then write the mobility tensor for $i, j = 1, 2$ as [106, Eq. (28)]

$$\mathbf{b}_{ij}^{\alpha\beta} = b_0 \delta_{ij} \delta^{\alpha\beta} + (1 - \delta_{ij}) \mathbf{G}^{\alpha\beta} (\mathbf{x}_i - \mathbf{x}_j). \quad (5.9)$$

This simplifies to

$$\mathbf{b}_{ij} = \begin{cases} \frac{1}{\gamma} \mathbf{I} & i = j \\ \frac{3a}{4r} \frac{1}{\gamma} \left(\mathbf{I} + \frac{\mathbf{r}\mathbf{r}}{r^2} \right) & i \neq j. \end{cases} \quad (5.10)$$

The velocity of particle i due to forces \mathbf{F}_j exerted on the two particles is

$$\mathbf{U}_i = \sum_{j=1}^2 \mathbf{b}_{ij} \cdot \mathbf{F}_j. \quad (5.11)$$

The interparticle velocity is then $d\mathbf{r}/dt = \mathbf{U}_2 - \mathbf{U}_1$. If the only forces acting on the particles arose from their mutual interactions, $\mathbf{F}_1 = -\mathbf{F}_2 = F \hat{\mathbf{r}}$. Thus

$$\begin{aligned} \frac{d\mathbf{r}_{\parallel}}{dt} &= (\mathbf{b}_{21} - \mathbf{b}_{11}) \cdot \mathbf{F}_1 + (\mathbf{b}_{22} - \mathbf{b}_{12}) \cdot \mathbf{F}_2 \\ &= 2F(\mathbf{b}_{21} - \mathbf{b}_{11}) \cdot \hat{\mathbf{r}}. \end{aligned} \quad (5.12)$$

By symmetry the relative velocity due to this interaction also is directed along $\hat{\mathbf{r}}$. Rewriting

$\mathbf{b}_{ij} = \mathbf{b}_{21}$ as

$$\mathbf{b}_{21} = \frac{1}{\gamma} \left[\frac{3a}{2r} \frac{\mathbf{r}\mathbf{r}}{r^2} + \frac{3a}{4r} \left(\mathbf{I} - \frac{\mathbf{r}\mathbf{r}}{r^2} \right) \right]$$

and applying the identity $(\mathbf{r}\mathbf{r}/r^2) \cdot \hat{\mathbf{r}} = \hat{\mathbf{r}}$, the relative velocity becomes

$$\frac{d\mathbf{r}_{\parallel}}{dt} = -\frac{2}{\gamma} \left(1 - \frac{3a}{2r} \right) F \hat{\mathbf{r}}. \quad (5.13)$$

Thermal forces contribute to relative motion both along $\hat{\mathbf{r}}$ and also along the perpendicular direction $\hat{\mathbf{r}}'$, which satisfies $\hat{\mathbf{r}}' \cdot \hat{\mathbf{r}} = 0$. We now apply the tensor identity $(\mathbf{rr}/r^2) \cdot \hat{\mathbf{r}}' = \mathbf{0}$ to obtain the relative velocity perpendicular to the particle separation:

$$\begin{aligned}\frac{d\mathbf{r}_\perp}{dt} &= 2F(\mathbf{b}_{21} - \mathbf{b}_{11}) \cdot \hat{\mathbf{r}}' \\ &= -\frac{2}{\gamma} \left(1 - \frac{3a}{4r}\right) F \hat{\mathbf{r}}'.\end{aligned}\tag{5.14}$$

This Stokeslet result is consistent with the pair mobilities derived in Ref. [107, §4] to first order in a/r .

We now have the mobility coefficient for the Langevin equation. Writing Eq. (5.2) in terms of the relative positions \mathbf{r}_\parallel and \mathbf{r}_\perp , we have the following one-dimensional equations

$$m \frac{d^2 r}{dt^2} = F_\parallel^\perp(r) - \frac{1}{\lambda_\parallel^\perp(r)} \frac{dr}{dt} + \Phi_\parallel^\perp(r, t),\tag{5.15}$$

where $\Phi(r, t)$ is the one-dimensional noise term $|\mathbf{f}_2(t) - \mathbf{f}_1(t)|$ in the relative motion frame and

$$\lambda_\parallel = \frac{2}{\gamma} \left(1 - \frac{3a}{2r}\right)\tag{5.16a}$$

$$\lambda_\perp = \frac{2}{\gamma} \left(1 - \frac{3a}{4r}\right)\tag{5.16b}$$

are the mobility terms derived in Eqs. (5.13) and (5.14).

5.1.3 Brownian dynamics

Completing our treatment of the Langevin equation requires an analysis of Brownian motion for a pair of particles. The Brownian force [9, Eqs. (3.5.4-5)] satisfies

$$\langle \mathbf{f}_i(t) \rangle = 0, \quad (5.17a)$$

$$\langle \mathbf{f}_i(t) \mathbf{f}_j(t') \rangle = F_{ij} \delta(t - t'). \quad (5.17b)$$

The coupling tensor F_{ij} is related to the friction tensor $f_{ij} = F_{ij}/(2k_B T)$ and obeys a relation similar to Eq. (5.11):

$$\mathbf{F}_i = \sum_{j=1}^2 f_{ij} \cdot \mathbf{U}_j. \quad (5.18)$$

As with the mobility tensor, this friction tensor depends on the interparticle separation.

The stochastic force vanishes on average for a system in thermodynamic equilibrium. Brownian forces are also uncorrelated on the time scale of the colloidal particle's motion, which accounts for the delta function in Eq. (5.17b). The tensor on the right hand side of Eq. (5.17b) is derived from the equipartition of kinetic energy along each translational normal mode:

$$\frac{1}{2}m \left\langle \frac{d\mathbf{x}_i}{dt} \frac{d\mathbf{x}_j}{dt} \right\rangle = \frac{1}{2}k_B T \delta_{ij} \mathbf{I}. \quad (5.19)$$

Integrating the Langevin equation to obtain the velocity of a single particle of mass m under the influence of a Brownian force $\mathbf{f}(t)$ reveals an exponential decay of information about initial conditions [9, Eq. (3.2.6)]:

$$\frac{d\mathbf{x}}{dt} = \frac{1}{m} \int_{-\infty}^t \mathbf{f}(t') \exp \left[-\frac{\gamma}{m}(t - t') \right] dt', \quad (5.20)$$

yielding the velocity autocorrelation function [9, Eq. (3.2.7)]

$$\begin{aligned} R(\tau) &= \left\langle \frac{d\mathbf{x}}{dt}(t) \frac{d\mathbf{x}}{dt}(t + \tau) \right\rangle \\ &= \frac{F_0}{2\gamma m} \exp\left[-\frac{\gamma}{m}\tau\right]. \end{aligned} \quad (5.21)$$

Setting $\tau = 0$ and comparing to Eq. (5.19) shows that

$$F_0 = 2k_B T \gamma \mathbf{I} = 2k_B T b_0^{-1}. \quad (5.22)$$

Fluctuation-dissipation tells us that a dissipative process that generates heat must contribute to a fluctuation, the increased Brownian motion of the particle as the heat dissipated into the system via viscous drag imparts kinetic energy to the molecules in the fluid. Indeed, Eq. (5.21) shows that Brownian forces become more vigorous as viscous drag increases. This makes sense when we examine the kinetic energy, as a particle must be driven by a stronger force in a more viscous fluid to maintain the same velocity magnitude. By integrating the velocity autocorrelation and applying Eq. (5.22), we find that the mean-squared displacement is related to a particle's diffusivity at time scales $t \gg \rho a^2/\eta$ greater than the viscous relaxation time,

$$\begin{aligned} \frac{1}{2} \langle \mathbf{x}(t) \mathbf{x}(t) \rangle &= k_B T b_0 t \mathbf{I} \\ &= D_0 t \mathbf{I}. \end{aligned} \quad (5.23)$$

Thus we retrieve the Einstein-Smoluchowski relation $D_0 = k_B T b_0$.

Let us now return to the relative motion frame in the two-particle case. We may write the Langevin equation for two identical spheres in a quiescent fluid in the absence of

interactions in terms of the friction tensor f_{ij} as

$$m \frac{d^2 \mathbf{x}_i}{dt^2} = - \sum_{j=1}^2 f_{ij} \cdot \frac{d \mathbf{x}_j}{dt} + \mathbf{f}_i. \quad (5.24)$$

The spheres' relative separation, $\mathbf{r} = \mathbf{x}_2 - \mathbf{x}_1$, then satisfies

$$m \frac{d^2 \mathbf{r}}{dt^2} = -f_r \cdot \frac{d \mathbf{r}}{dt} + \mathbf{f}_2 - \mathbf{f}_1, \quad (5.25)$$

where $f_r = f_{11} - f_{12}$. Equipartition then yields

$$\begin{aligned} \frac{1}{2} m \left\langle \frac{d \mathbf{r}}{dt} \frac{d \mathbf{r}}{dt} \right\rangle &= \frac{1}{2} m \left(\left\langle \frac{d \mathbf{x}_1}{dt} \frac{d \mathbf{x}_1}{dt} \right\rangle + \left\langle \frac{d \mathbf{x}_2}{dt} \frac{d \mathbf{x}_2}{dt} \right\rangle \right) \\ &= k_B T \mathbf{I}. \end{aligned} \quad (5.26)$$

Applying a similar analysis as we did in the single-particle case by using Eq. (5.17), Eq. (5.19) and Eq. (5.26), we obtain the following results [9, Eqs. (3.5.10-11)]:

$$F_{ij} = 2k_B T f_{ij}, \quad (5.27a)$$

$$R_r(\tau) = \frac{4k_B T}{m} \exp \left[-f_r \frac{\tau}{m} \right], \quad (5.27b)$$

$$\frac{1}{2} \langle \mathbf{r}(t) \mathbf{r}(t) \rangle = 2k_B T f_r^{-1} t = D(\mathbf{r}) t, \quad (5.27c)$$

where $D(\mathbf{r})$ is the diffusivity tensor. The inverse relative motion friction tensor f_r^{-1} can be written in terms of the mobility tensor b_{ij} as $f_r^{-1} = b_{11} - b_{12}$. Thus we have a relation between the mobility and diffusivity,

$$D(\mathbf{r}) = 2k_B T (b_{11}(\mathbf{r}) - b_{12}(\mathbf{r})). \quad (5.28)$$

Using the results from §5.1.2, this corresponds to the following values for D in the parallel and perpendicular normal modes:

$$D_{\parallel}^{\perp}(r) = k_B T \lambda_{\parallel}^{\perp}(r), \quad (5.29)$$

where $\lambda_{\parallel}^{\perp}$ are the perpendicular and parallel mobilities.

We have seen in §5.1.2 that the mobility drops as the particles approach one another, which is akin to an increase in the viscous drag. As a result of this, the Brownian forces would have to increase to maintain a constant kinetic energy.

By combining the results of this and the previous sections, we arrive at a final expression for the Langevin equation in the parallel and perpendicular normal modes,

$$m \frac{d^2 r}{dt^2} = F_{\parallel}^{\perp}(r) - \frac{k_B T}{D_{\parallel}^{\perp}(r)} \frac{dr}{dt} + \Phi_{\parallel}^{\perp}(r, t), \quad (5.30)$$

where $\Phi_{\parallel}^{\perp}(r, t)$ satisfies

$$\begin{aligned} \langle \Phi_{\parallel}^{\perp}(r, t) \rangle &= 0, \\ \langle \Phi_{\parallel}^{\perp}(r, t) \Phi_{\parallel}^{\perp}(r, t') \rangle &= 2 D_{\parallel}^{\perp}(r) \delta(t - t'). \end{aligned}$$

In the creeping flow or overdamped limit, inertial forces are negligible compared to the drag force. Time averaging the result, we are left with

$$\bar{F}_{\parallel}^{\perp}(r) = k_B T \frac{\bar{v}_{\parallel}^{\perp}(r)}{\bar{D}_{\parallel}^{\perp}(r)}. \quad (5.31)$$

These equations are a direct result of the one-dimensional Smoluchowski equation, which is solved by a Gaussian distribution, provided that $D' \ll v$ [41]. Our trajectory data en-

sembles provide the necessary ingredients for computing the average velocity, diffusivity, and force [36, 41–43].

5.2 Kernel Density Estimation

One standard method of extracting the velocity and diffusivity from trajectory data is to fit histograms to known Gaussian distributions of the displacement Δr for various time intervals Δt . In the case of particles with an initial separation r diffusing with drift velocity v and diffusivity D , a histogram of Δr would have the form [41, Eq. (5)]

$$N(r, \Delta r, \Delta t) = N_0 \exp \left[-\frac{(\Delta r - \overline{\Delta r})^2}{2\sigma_{\Delta r}^2} \right], \quad (5.32)$$

where $\overline{\Delta r} = v\Delta t$ and $\sigma_{\Delta r}^2 = 2D\Delta t$. The parameters in these fits are the mean displacement $\overline{\Delta r}$ and the mean-squared displacement $\sigma_{\Delta r}^2$, each varying linearly with respect to Δt . The slope of the mean displacement with respect to Δt is the velocity v for a given initial separation r . Likewise, the slope of the mean squared displacement is $2D$. This two-step fitting method of extracting transport coefficients v and D with respect to r is known as **parametric density estimation** [108, §1.1] and is employed in Ref. [41, Fig. 1(b)-(c)].

Parametric density estimates assume a specific functional form for the probability density from which to extract relevant constants, in this case a Gaussian form like Eq. (5.32). We define the **probability density** as the function f such that the probability of a random quantity X to occur between a and b for all $a < b$ is

$$P(a < X < b) = \int_a^b f(x) dx.$$

The density function f is a description of the statistical distribution of X . **Density estimation** is the process by which we reconstruct f from a set of data. A **nonparametric** approach to density estimation allows us to make no assumptions regarding the form that f takes, so that no curve fitting is necessary to extract ensemble averages of quantities such as v and D in our case.

The histogram is one commonly used (and abused) density estimator. For a given set of N data points $\{X_i\}$ between x_0 and x_f , we may construct a histogram of bin width h such that the bins consist of intervals $[x_0 + (m - 1)h, x_0 + mh)$, where $m = 1, 2, \dots, n = (x_f - x_0)/h$. The bin width h is chosen such that $(x_f - x_0)/h$, or the number of bins within the interval $[x_0, x_f]$, is an integer. The histogram itself is defined as

$$\hat{f}(x) = \frac{1}{Nh} \text{(number of } X_i \text{ in the same bin as } x). \quad (5.33)$$

Depending on the volume of data, the shape of $\hat{f}(x)$ will depend heavily on the size and origin of the bins. Silverman [108, §2.2] argues that while the histogram is a valuable tool for presenting statistical data, arbitrary noisiness caused by the binning process make histograms a poor choice for estimating derivatives or ratios of density estimates.

Rather than binning trajectory data to estimate $v(r)$ and $D(r)$, we improve statistical sampling by using adaptive kernel density estimators [108, §2.4]. For a histogram, each bin X_i represents a step function of width h and height $(Nh)^{-1}$. As a result, any trajectory information that may exist between adjacent bins in x would be lost. While we may gain some data resolution between bins by narrowing h , the discrete nature of binning makes for a discontinuous density estimate. Instead of representing each data point as a step

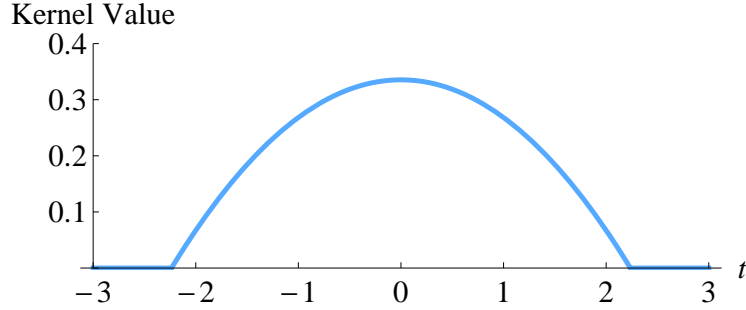


Figure 5.1: The Epanechnikov kernel

function, we use a **kernel function** K , which satisfies [108, Eq. (2.2)]

$$\int_{-\infty}^{\infty} K(x) dx = 1. \quad (5.34)$$

The kernel function may take many forms and need not be symmetric, but for our purposes, we will use the **Epanechnikov kernel** [109] defined as

$$K_e(t) = \begin{cases} \frac{3}{4\sqrt{5}} \left(1 - \frac{1}{5}t^2\right) & -\sqrt{5} \leq t \leq \sqrt{5} \\ 0 & \text{otherwise.} \end{cases} \quad (5.35)$$

Quantitatively equivalent results may also be obtained with other kernel choices, including triangular, biweight, or Gaussian kernels [108, §3.3.2].

We may now construct a **kernel density estimator** (KDE), which is the sum of the kernel functions representing each data point X_i :

$$f(x) = \frac{1}{Nh_e} \sum_{i=1}^N K_e \left(\frac{x - X_i}{h_e} \right). \quad (5.36)$$

In this equation, h_e is a smoothing parameter or **window width**, which determines the width of the kernel. As h_e increases, the density function becomes smoother. This smooth-

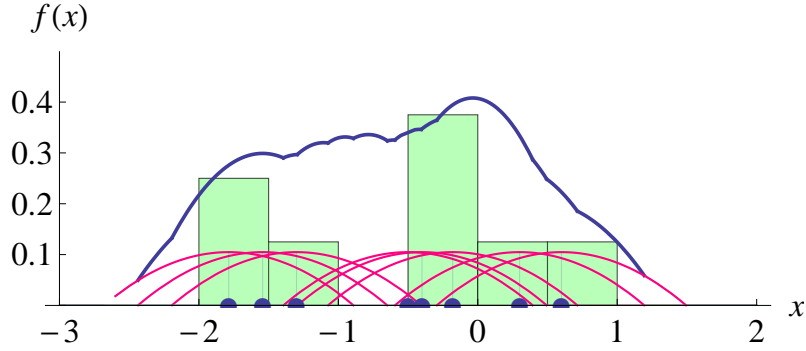


Figure 5.2: Normalized histogram of sample data with bin size $h = 0.5$ plotted against a kernel density estimate using the Epanechnikov kernel with $h_e = 0.4$.

ing parameter may be arbitrary chosen, or it may depend on the local density of data points. A sample density function using the Epanechnikov kernel is shown in Fig. 5.2. Even with a set of eight data points, we have a better understanding of how the data is distributed with a kernel density estimator than we would with a histogram.

Adaptive kernel density estimators (AKDEs) employ variable window widths proportional to the distance d_{ij} between X_i and the j th nearest point in the data set. The density function is now [108, Eq. (2.5)]

$$f(x) = \frac{1}{N} \sum_{i=1}^N \frac{1}{h_e d_{ij}} K_e \left(\frac{x - X_i}{h_e d_{ij}} \right). \quad (5.37)$$

The adjustable kernel width allows for wider kernels in low-density data regions and narrower kernels for high-density regions. This exposes more detail in data-rich regions while smoothing out noise in sparse regions.

5.2.1 Position and velocity estimates

Applying kernel density estimators to our data involves finding a density estimate of the set $\{r_{j,n}\}$ of one-dimensional position data gridded at time intervals $n\tau$ that we found in Eq. (4.10b). Such a density estimate is given by

$$\rho_n(r) = \frac{1}{N-n} \sum_{j=1}^{N-n} \frac{1}{h_j} K\left(\frac{r - r_{j,n}}{h_j}\right), \quad (5.38)$$

where K is the Epanechnikov kernel of width h_j . One such density function for $n = 1$ is shown in Fig. 5.3. The shape of the KDE for our data is mostly arbitrary, as it depends on initial particle separations during the data gathering phase. Data is densest where particles are close and repel each other and sparse where particles are far apart and mostly diffuse. At extremely close proximity however, the particles spend so little time near each other that data collected at these separations is also sparse. The shape of $\rho(r)$ becomes important when we use it to normalize the weighted density functions necessary to calculate $v(r)$ and $D(r)$. Figure 5.3 also displays how the choice of bins drastically affects the shape of the density histogram, whereas the difference between kernel and adaptive kernel estimates for this sample is small.

Despite the robustness of KDEs for generating accurate density functions, statistical errors are still unavoidable. The uncertainty estimate $\Sigma_{w_n}(r)$ of the density function generated by weighted data $\{w_{j,n}\}$ is given by

$$\Sigma_{w_n}(r) = \sqrt{\frac{1}{N-n} \sum_{j=1}^{N-n} \left[w_{j,n} \frac{1}{h_j} K\left(\frac{r - r_{j,n}}{h_j}\right) \right]^2}. \quad (5.39)$$

This error estimate has the form of a functional standard deviation from the weighted

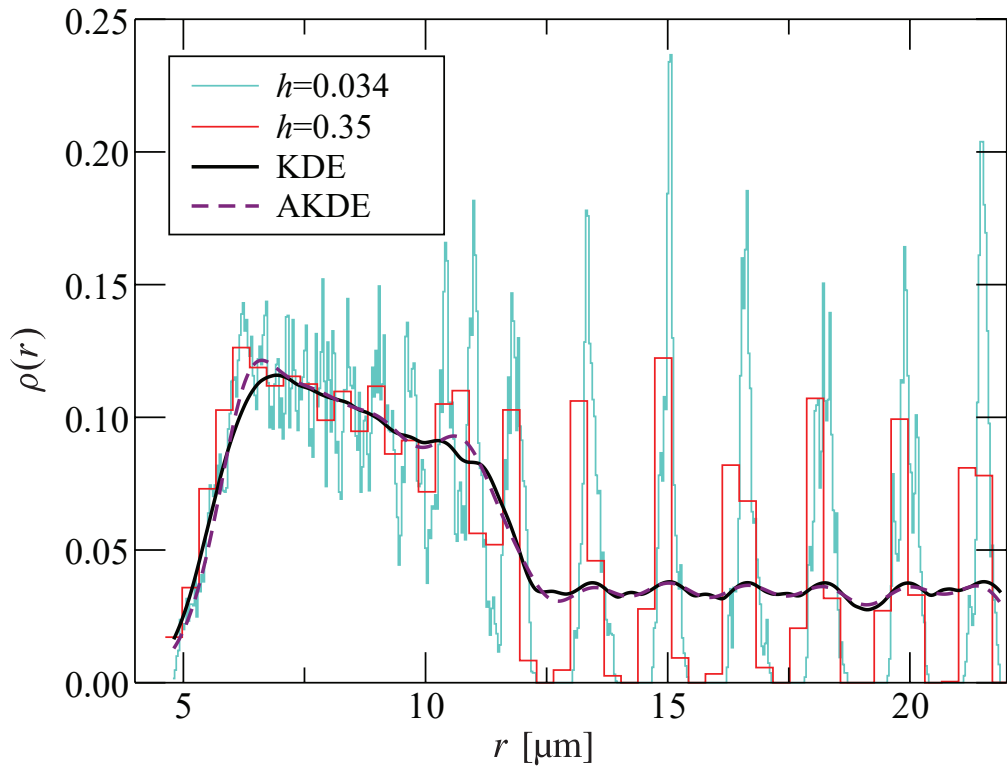


Figure 5.3: Probability distribution function for positions of 2.3 μm -diameter PMMA spheres. Normalized histogram and kernel density estimates compared. The kernel density estimate (solid black line) employs the Epanechnikov kernel and the adaptive kernel estimate (dashed purple line) employs a Gaussian kernel.

average

$$\bar{w}_n(r) = \frac{1}{N-n} \sum_{j=1}^{N-n} w_{j,n} \frac{1}{h_j} K\left(\frac{r - r_{j,n}}{h_j}\right).$$

For an unweighted density function $\rho_n(r)$, the error estimate $\Sigma_{\rho_n}(r)$ is simply Eq. (5.39) with $w_{j,n} = 1$. Propagating errors in $\rho_n(r)$ and $\bar{w}_n(r)$ yields the statistical uncertainty of the normalized density function $\hat{w}_n(r) = \bar{w}_n(r)/\rho_n(r)$:

$$\delta \hat{w}_n(r) = |\bar{w}_n(r)| \sqrt{\left(\frac{\Sigma_{w_n}(r)}{\bar{w}_n(r)}\right)^2 + \left(\frac{\Sigma_{\rho_n}(r)}{\rho_n(r)}\right)^2}. \quad (5.40)$$

The average velocity at separation r can be obtained with density estimates weighted by the n -step velocity values $v_{j,n}$ measured at separation $r_{j,n}$ and normalizing it as we did for $\{w_{j,n}\}$ above. The normalized weighted density estimate for a set $\{v_{j,n}\}$ of one-dimensional velocity data is

$$\bar{v}_n(r) = \frac{1}{\rho_n(r)} \frac{1}{N-n} \sum_{j=1}^{N-n} v_{j,n} \frac{1}{h_j} K\left(\frac{r - r_{j,n}}{h_j}\right). \quad (5.41)$$

By applying Eqs. (5.41) and (5.40) on the data in Fig. 5.3, we obtain the relative velocity profile with error estimates shown in Fig. 5.4. Because our system is Markovian, the interparticle velocity of the spheres at a given separation r is independent of their initial separation r_i during the data collection phase. In practice, the velocity profile is smooth and well-resolved for separations ranging up to four particle diameters. The perpendicular velocity contribution $v^\perp(r)$ is small compared to $v^\parallel(r)$. This is consistent with the absence of external forces and with a central force acting between the spheres.

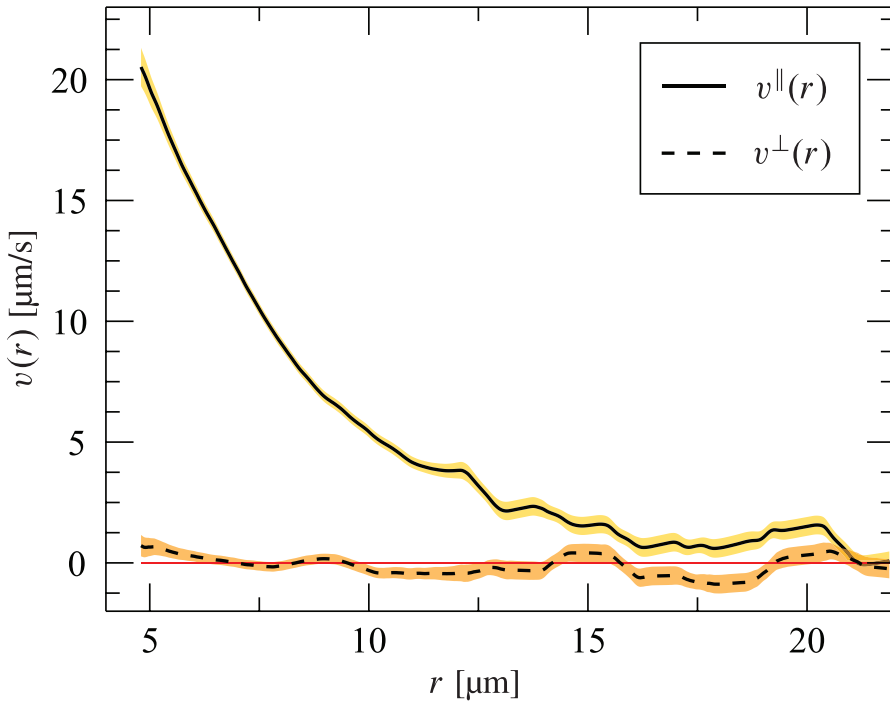


Figure 5.4: Average relative velocity of 2.3 μm -diameter PMMA spheres as a function of interparticle separation in the parallel (solid line) and perpendicular (dashed line) modes. Shaded regions are statistical uncertainties of the velocity estimates.

5.3 Diffusivity Estimates

The standard method for finding the pair diffusivity from a set of trajectory data is to calculate the relative mean-squared displacement (MSD) $\langle(\Delta r)^2\rangle$ for various values of the lag time Δt . The Einstein relation, Eq. (5.23), then yields the pair diffusivity

$$D(r) = \frac{\langle(\Delta r)^2\rangle}{2\Delta t}.$$

However, there are a few issues with this method for our purposes. First of all, the duration of each blink is too short for us to build meaningful statistics for the MSD in this manner. There will not be enough values for Δt over which to obtain an accurate estimate for $D(r)$

at each initial separation r . Second, hydrodynamic coupling between a pair of spheres will affect how they diffuse with respect to their relative separation. The closer the spheres are to each other, the more their pair diffusivity will deviate from $2D_0$, the Stokes-Einstein relation for two spheres. As we have shown in §5.1.3, the pair mobility and thus the diffusivity has a separation dependence governed by

$$D_{\parallel}(r) = 2D_0 \left[1 - \frac{3}{2} \frac{a}{r} + \mathcal{O}\left(\left(\frac{a}{r}\right)^3\right) \right], \quad (5.42a)$$

$$D_{\perp}(r) = 2D_0 \left[1 - \frac{3}{4} \frac{a}{r} + \mathcal{O}\left(\left(\frac{a}{r}\right)^3\right) \right], \quad (5.42b)$$

where $D_0 = k_B T / \gamma$ is the single-sphere diffusion constant. We will show how a diffusivity profile calculated from our trajectory data agrees with this behavior without having to make any assumptions about the particles' hydrodynamic interactions.

5.3.1 Diffusivity profile

We obtain the diffusion coefficient from estimates for the velocity fluctuations by calculating the velocity variance

$$\begin{aligned} \overline{\Delta v_n^2}(r) &= \frac{1}{\rho_n(r)} \frac{1}{N-n} \sum_{j=1}^{N-n} (v_{j,n} - \bar{v}_n(r))^2 \frac{1}{h_j} K\left(\frac{r - r_{j,n}}{h_j}\right) \\ &= \frac{1}{\rho_n(r)} \frac{1}{N-n} \sum_{j=1}^{N-n} v_{j,n}^2 \frac{1}{h_j} K\left(\frac{r - r_{j,n}}{h_j}\right) - \bar{v}_n^2(r). \end{aligned} \quad (5.43)$$

These mean-squared velocity fluctuations are then related to the pair diffusivity by applying the Einstein-Smoluchowski relation:

$$\overline{\Delta v_n^2}(r) = \frac{2}{n\tau} D(r) + \frac{2}{n^2\tau^2} \epsilon^2(r), \quad (5.44)$$

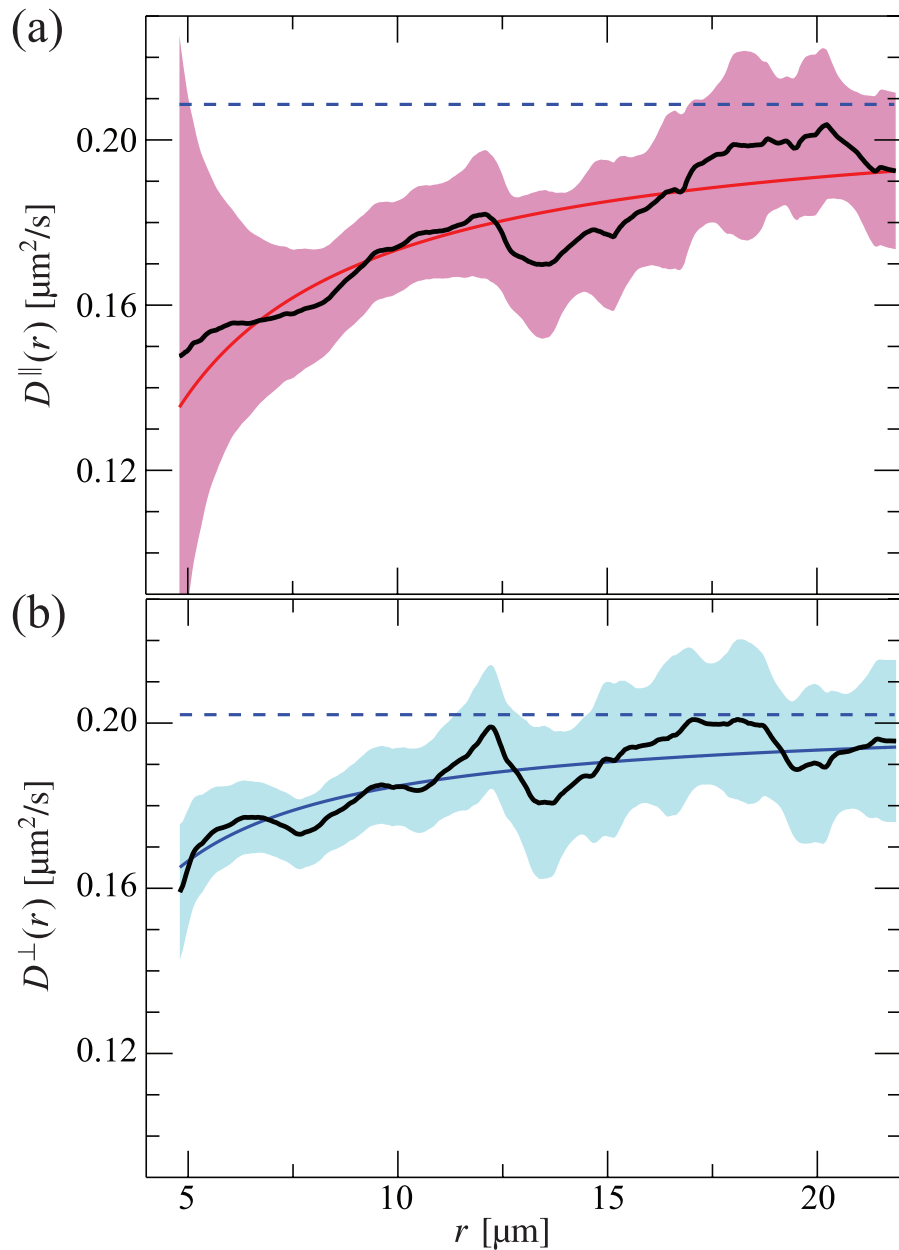


Figure 5.5: Average relative diffusivity of 2.3 μm -diameter PMMA spheres as a function of interparticle separation in **(a)** the parallel mode and **(b)** the perpendicular mode. Colored curves indicate theoretical predictions given by Eq. (5.42). The dashed lines indicate the asymptotic diffusivity $2D_0$. Shaded regions represent statistical uncertainties.

where $\epsilon(r)$ is the measurement error in the pair separation [40, 97, 110], which may depend on the separation. As discussed in §4.1, these errors are most likely caused by the finite exposure time it requires to capture an image. Assuming that $\epsilon(r)$ has zero mean, these errors should not affect the estimate for $\bar{v}_n(r)$. Measurement errors, though they depend on the exposure time, should not depend on how we sample the data once they are collected. Hence, there is no n -dependence for $\epsilon(r)$ in Eq. (5.44). We may estimate the separation-dependent relative diffusivity from any pair of estimators calculated with sample intervals n and n' as

$$\overline{D}(r) = \tau \frac{\overline{\Delta v_{n'}^2}(r) n'^2 - \overline{\Delta v_n^2}(r) n^2}{2(n' - n)}. \quad (5.45)$$

As discussed in the beginning of this chapter, greedy sampling should not affect estimates for $v(r)$ or $D(r)$ provided that the trajectories may be treated as Markov processes. This, in turn, requires that the time interval $n\tau$ be short enough that relative changes in the underlying force and mobility are small enough to be ignored. Indeed, the Reynolds number for our system is sufficiently small for us to safely assume that this system is Markovian, especially when we consider the high framerate at which we acquire images ($\tau = 1/1500$ s).

An estimate for the pair interaction, $\overline{F}(r)$, can be obtained from $\bar{v}(r)$ and $\overline{D}(r)$ using Eq. (5.31). The data in Fig. 5.5 show results for a typical data set obtained with $n = 1$ and $n' = 2$ in the (a) parallel and (b) perpendicular normal modes of motion. Both curves approach the asymptotic diffusion constant $2D_0$, indicated by dashed lines in Fig. 5.5. The solid red curve in Fig. 5.5(a) is a one-parameter fit to leading-order prediction of Eq. (5.42a):

$$D^{\parallel}(r) = 2D_0 \left[1 - \frac{3}{2} \frac{a_p}{r} + \mathcal{O}\left(\left(\frac{a_p}{r}\right)^3\right) \right].$$

The fit value $D_0 = (0.104 \pm 0.004) \mu\text{m}^2/\text{s}$ is consistent with the Stokes-Einstein value, $D_0 = k_{\text{B}}T/(6\pi\eta_0 a_p) = (0.096 \pm 0.005) \mu\text{m}^2/\text{s}$, using the value for η_0 from Table 3.1. Similarly, we may extract a value of D_0 from a fit of the perpendicular mode diffusivity, indicated by the solid blue curve in Fig. 5.5(b), from Eq. (5.42b),

$$D^\perp(r) = 2D_0 \left[1 - \frac{3}{4} \frac{a_p}{r} + \mathcal{O}\left(\left(\frac{a_p}{r}\right)^3\right) \right].$$

This fit yields $D_0 = (0.101 \pm 0.004) \mu\text{m}^2/\text{s}$, also consistent with previous results for D_0 .

5.4 Force and Potential Estimates

Combining estimates for the relative velocity $\bar{v}(r)$ with the relative pair diffusivity $\bar{D}(r)$ yields an estimate for the interparticle force $\bar{F}(r)$, as per Eq. (5.31). Results for both the parallel and perpendicular modes are plotted in Fig. 5.6. As is typical for all of the particle pairs measured, these spheres repel each other with a force that falls off with increasing separation in the parallel normal mode. The interparticle force is negligible in the perpendicular mode.

At least as a point of departure, it seems reasonable to compare these results with the predictions of the linearized Poisson-Boltzmann theory for colloidal electrostatic interactions in simple electrolytes, discussed in Ch. 2. Any discrepancies then would cast light on ways in which the CXB-dodecane system departs from this idealized model and on unusual charging mechanisms for the spheres. The pair interaction between identical particles then can be described as a screened-Coulomb repulsion, as we derived in §2.3,

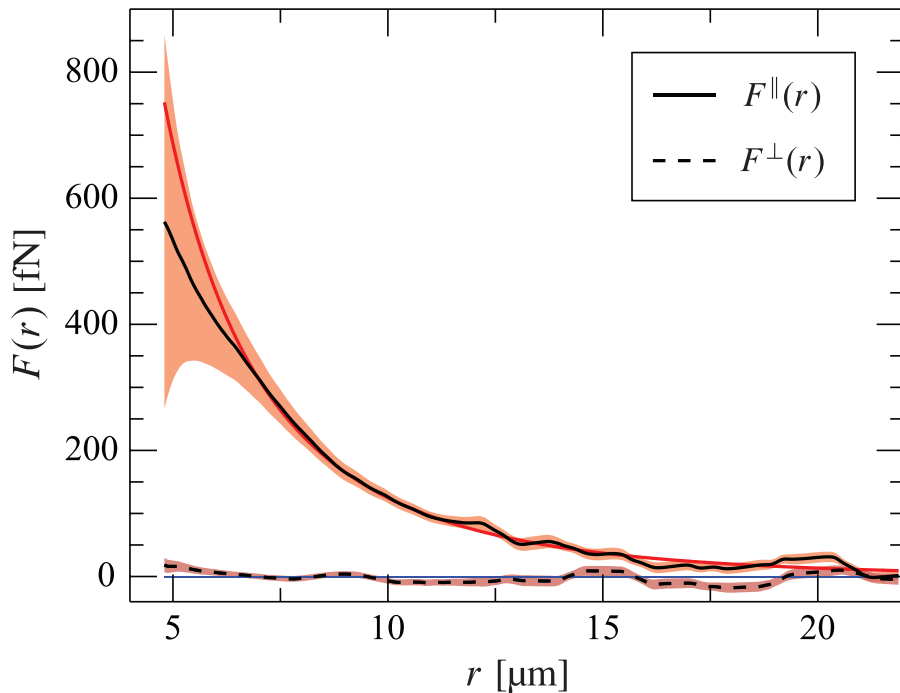


Figure 5.6: Average interparticle forces of 2.3 μm -diameter PMMA spheres as a function of interparticle separation in the parallel (solid line) and perpendicular (dashed line) modes. The red curve is a fit to the screened-Coulomb force given by Eq. (2.10). Shaded regions represent statistical uncertainties.

written in terms of the Bjerrum length λ_B introduced in Eq. (1.1),

$$U_{sc}(r) = k_B T Z^{*2} \lambda_B \left(\frac{e^{\kappa a_p}}{1 + \kappa a_p} \right)^2 \frac{e^{-\kappa r}}{r}, \quad (5.46)$$

where Z^* is the effective charge number on each sphere. In conventional aqueous electrolytes, the squared term in Eq. (5.46) accounts for the exclusion of simple ions from the spheres' interior. The red curve in Fig. 5.6 is a two-parameter fit to

$$F_{sc}(r) = \left(\frac{1}{r} + \kappa \right) U_{sc}(r) \quad (5.47)$$

for the spheres' effective charge number, $Z^* = 701 \pm 23$, and the electrolyte's screening length in the presence of spheres, $\kappa_s^{-1} = (7.7 \pm 0.1) \mu\text{m}$. Consistent values for the effective charge have been inferred from the pair correlation function of similar many-sphere dispersions [104].

The screening length estimated from the spheres' interactions is significantly larger than the bulk value $\kappa_b^{-1} = (3.4 \pm 0.1) \mu\text{m}$ estimated from the solvent's conductivity. The ratio of the respective ionic strengths is

$$\frac{n_s}{n_b} = \left(\frac{\kappa_b^{-1}}{\kappa_s^{-1}} \right)^2 \approx \frac{1}{3}.$$

This may be explained if the functionalized PMMA spheres acquire their charges by adsorbing cations from solution as per our discussion in 3.1.3. The immobilized spheres that are deposited on the walls then prevent these ions from contributing to charge transport.

Comparably good results are obtained for pairs of spheres ranging from $a_p = 0.55 \mu\text{m}$ to $a_p = 2.70 \mu\text{m}$. To more easily compare these measurements, we compute the in-

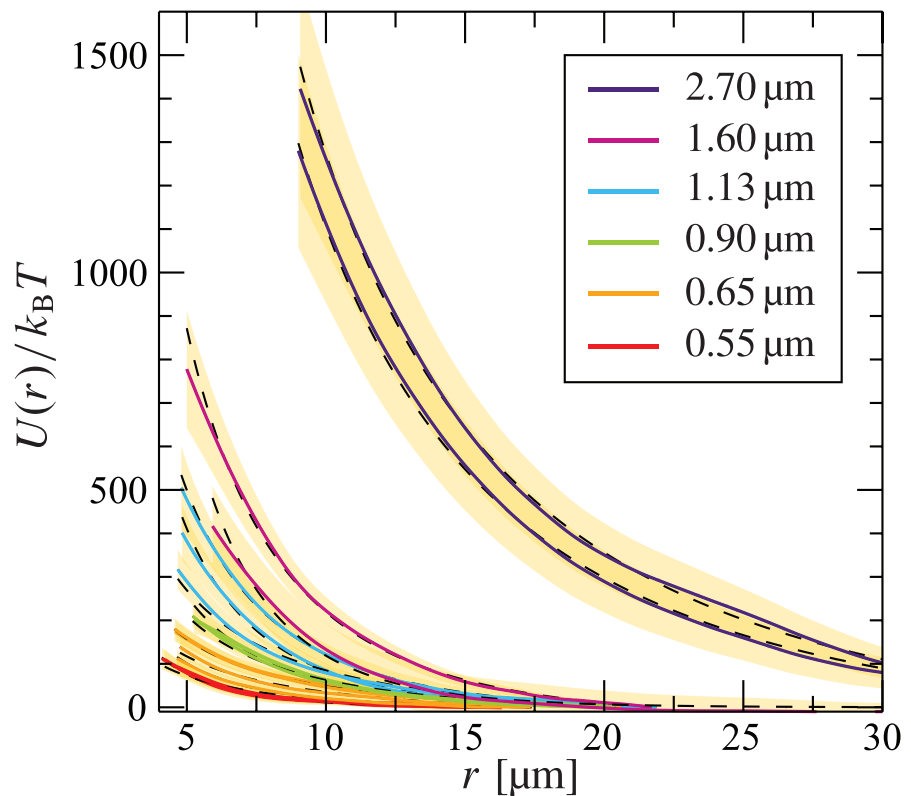


Figure 5.7: Pair potentials $U_{\text{sc}}(r)$ in units of the thermal energy scale for spheres of various particle radii a_p obtained by numerically integrating measured pair forces. Dashed lines are fit curves from the screened-Coulomb potential given by Eq. (5.46). Shaded regions represent statistical uncertainties.

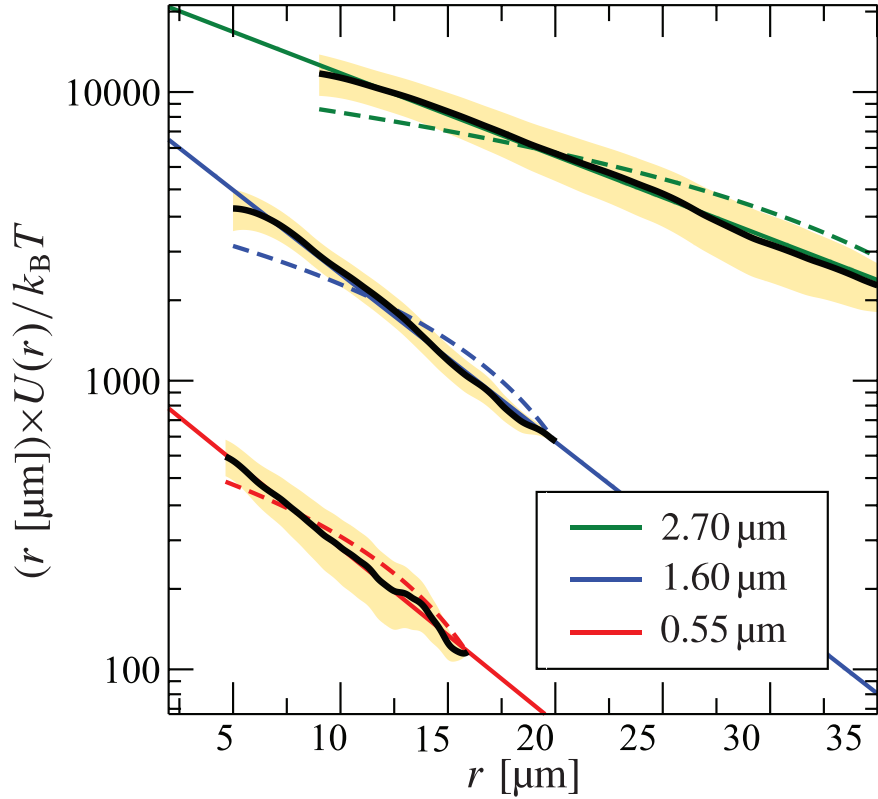


Figure 5.8: Selected data from Fig. 5.7 replotted to emphasize the screen-Coulomb form. Solid curves represent fits to the screened-Coulomb potential, while dashed curves are fits to pure Coulomb repulsion. Shaded regions represent statistical uncertainties.

terparticle potential $U_{sc}(r)$ by numerically integrating $F_{sc}(r)$ under the assumption that $\lim_{r \rightarrow \infty} U_{sc}(r) = 0$. Figure 5.7 shows results for 16 pairs of spheres (solid curves) together with statistical uncertainties (shaded regions) and fits to Eq. (5.46) (dashed curves). To emphasize the agreement between these measurements and theory, we re-plot representative curves in Fig. 5.8 so that the screened-Coulomb form falls on a line whose slope is κ . For comparison, we also plot the best fit to a pure Coulomb repulsion ($\kappa = 0$) as dashed curves.

5.5 Charges

How the spheres' charges depend on their radii offers insights into their charging mechanism. Figure 5.9(a) shows how Z^* scales with a_p for the data in Fig. 5.7. The discrete points in Fig. 5.9(b) show fit values for $Z^*(a_p)$ plotted as a function of the fit values of the reduced radius κa_p . These results are scaled to emphasize the relationship between effective surface charge and effective potential, ζ^* , that is predicted by charge renormalization theory [44, 98, 111, 112],

$$Z^* \frac{\lambda_B}{a_p} = \left| \frac{e\zeta^*}{k_B T} \right| (1 + \kappa a_p). \quad (5.48)$$

The good agreement between our measurements and a one-parameter fit of the data to Eq. 5.48 for the effective surface potential $e\zeta^* = (5.2 \pm 0.4)k_B T$ suggests that the spheres' charges are regulated by a constant surface potential.

The observed linear dependence of Z^* on a_p contrasts with a recent report [76] of complementary measurements on the same system prepared with a higher volume fraction of particles. The quadratic dependence of the effective charge number on the particle radius reported in that study is inconsistent with Eq. (5.48). Having the effective charge be proportional to the surface area could be consistent with charging controlled by the chemical equilibria of weak association and dissociation reactions [113]. Our measurements, by contrast, are consistent with standard thermodynamic mechanisms [73] in a conventional electrolyte, at least for spheres at a very low volume fraction.

The large screening length of the CXB-dodecane mixture creates an additional way to probe the spheres' charging mechanism. As discussed in §2.4, charges on small spheres ($\kappa a_p < 1$) are limited by counterion condensation. The limiting condition in the case of

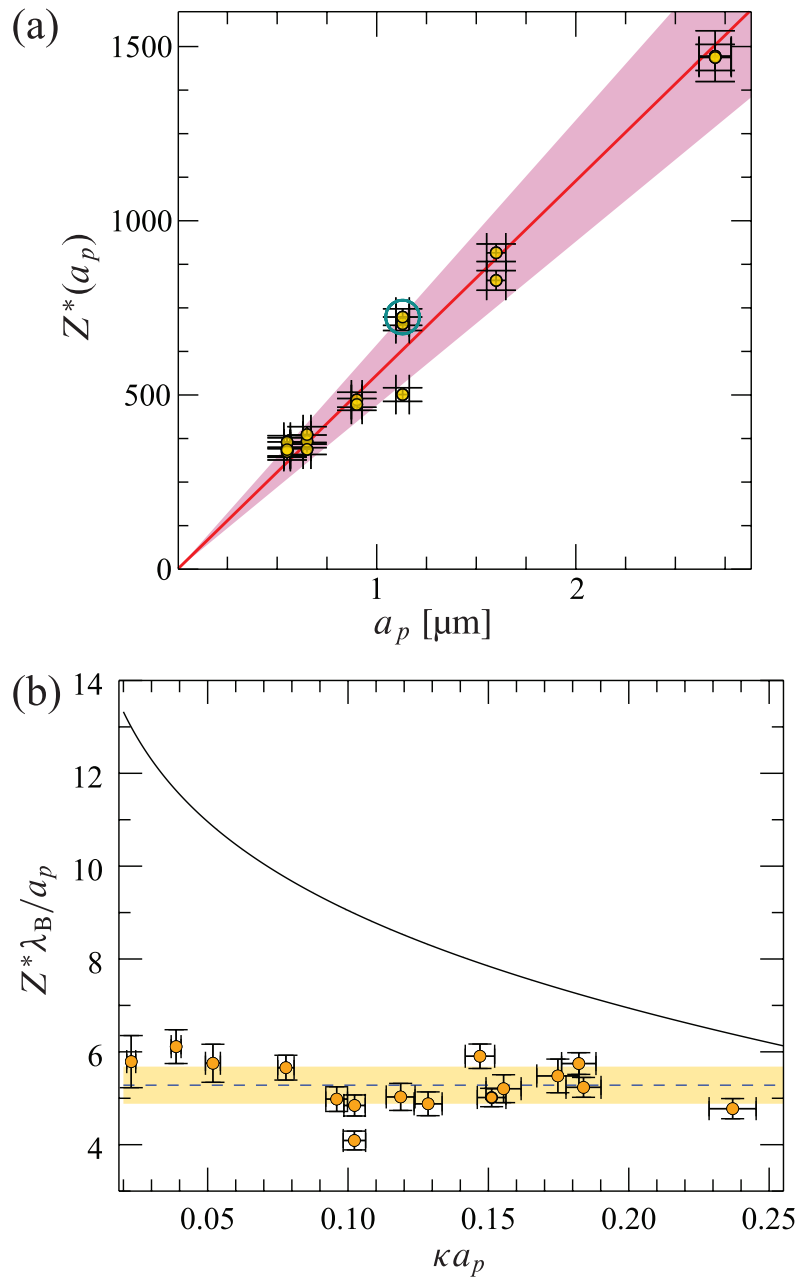


Figure 5.9: (a) Effective charge number $Z^*(a_p)$ of PMMA spheres suspended in CXB-dodecane with respect to particle radius a_p . Shaded region indicates error of the slope of the linear least-square fit to the data. (b) Effective charge number Z^* with respect to the reduced particle size κa_p . The solid curve is the limiting effective charge from Eq. (5.49). The dashed horizontal line indicates the mean effective surface potential of $5.2k_B T$ and the shaded region indicates the uncertainty in this value of $\pm 0.4k_B T$.

spheres dispersed in a 1 : 1 electrolyte is given by Eq. (2.12):

$$Z^* \frac{\lambda_B}{a_p} < 4 \ln 2 - 2 \ln \kappa a_p + 2 \ln(-\ln \kappa a_p) \\ - \frac{1}{2} \ln \left(\frac{Z \lambda_B / a_p - 2 \ln \kappa a_p}{Z \lambda_B / a_p + 2 \ln \kappa a_p} \right) + \mathcal{O}\{1\}, \quad (5.49)$$

where Z is the sphere's bare charge. This result recently has been shown to be consistent with the measured electrophoretic mobility of highly charged colloidal spheres [114]. Predictions for the present system in the limit of large bare charge are plotted as the solid curve in Fig. 5.9(b). The measured values all being well below the Poisson-Boltzmann limit as derived by Ramanathan [47], we conclude that the spheres' effective charges are not reduced by charge renormalization and thus should differ little from the bare charges.

This conclusion is further supported by referring to analytical expressions for the full Poisson-Boltzmann potential outside a charged sphere [115]. In the domain of the present experiments, $\kappa a_p < 0.3$, $e\zeta^* < 6k_B T$, and $\kappa r \gtrsim 1$, the linearized Poisson-Boltzmann approximation overestimates the potential energy for monovalent ions at distance r from the charged sphere's center by less than 1% [115, Eq. (8)]. Assuming that the potential energy for a charged sphere centered at the same large separation can be obtained by linear superposition, our fits to experimental estimates for $U(r)$ would thus underestimate the spheres' surface potentials by far less than the experimental uncertainty. The fit values for the effective charges on the spheres would thus should be reasonably good estimates for their bare charges, $Z^* \approx Z$.

5.6 Conclusions

Based on these considerations, we propose that the spheres in the present study acquire their charges by association of cations from solution. The presence in solution of protons from the dehydrobromination of CXB suggests a likely source for those cations. With this interpretation, the measured surface potential of $5k_B T$ reasonably corresponds to the energy of association between the cations and polarizable groups bound to the spheres' surfaces. This potential is below the threshold for charge condensation. Few counterions, therefore, are likely to be associated with the surface. Spheres that are substantially larger than those in the present study might cross over into the regime of strong charge renormalization. Whether that would take the form of cation dissociation or counterion condensation is an open question.

The outstanding puzzle in the present study is how the CXB-dodecane electrolyte appears to be rather conventional. Both conductivity and colloidal interaction measurements suggest the presence of free ions in solution, even though the energetic cost of charge separation should be substantially higher than the thermal energy scale. No organic salt or charge-stabilization agents were added to the suspension, nor are any of the system's components likely to form nanoscale structures such as inverse micelles that would allow for stable charge separation at room temperature [5]. The same mechanism that allows for separation of hydrogen and bromide ions in solution is likely to be involved in charging the PMMA spheres. Once they are more fully understood, such organic electrolyte systems will provide interesting model systems with which to study electrostatic coupling in charge-stabilized colloidal dispersions. The high charges and long screening lengths that can be attained will be useful for probing nonlinear screening and the breakdown of

pairwise additivity in charged spheres' electrostatic interactions. Understanding and controlling charge transfer mechanisms in simple organic electrolytes such as CXB-dodecane may yield useful alternatives to aqueous electrolytes in practical applications.

References

- [1] P. N. Pusey and W. van Megen, “Phase behaviour of concentrated suspensions of nearly hard colloidal spheres,” *Nature* **320**, 340–342 (1986).
- [2] E. J. W. Verwey and J. T. G. Overbeek, *Theory of the Stability of Lyophobic Colloids: The Interactions of Sol Particles Having an Electric Double Layer* (Elsevier, New York, 1948).
- [3] A. Kose, M. Ozaki, K. Takano, Y. Kobayashi, and S. Hachisu, “Direct observation of ordered latex suspension by metallurgical microscope,” *J. Colloid Interface Sci.* **44**, 330–338 (1973).
- [4] J. O. Bockris and A. K. N. Reddy, *Modern Electrochemistry* (Plenum Press, New York, 1970).
- [5] M. F. Hsu, E. R. Dufresne, and D. A. Weitz, “Charge stabilization in nonpolar solvents,” *Langmuir* **21**, 4881–4887 (2005).
- [6] R. M. Fuoss, “Ionic Association. III. The Equilibrium between Ion Pairs and Free Ions,” *J. Am. Chem. Soc.* **80**, 5059–5061 (1958).
- [7] I. D. Morrison, “Electrical charges in nonaqueous media,” *Colloids Surf. A* **71**, 1–37 (1993).
- [8] T. Graham, “X. Liquid Diffusion applied to Analysis,” *Philos. Trans. Roy. Soc. London* **151**, 183–224 (1861).
- [9] W. B. Russel, D. A. Saville, and W. R. Schowalter, *Colloidal Dispersions*, Cambridge Monographs on Mechanics and Applied Mathematics (Cambridge University Press, Cambridge, UK, 1989).
- [10] M. Faraday, “The Bakerian Lecture: Experimental relations of gold (and other metals) to light,” *Philos. Trans. Roy. Soc. Lond.* **147**, 145–181 (1857).
- [11] H. Siedentopf and R. Zsigmondy, “Über Sichtbarmachung und Größenbestimmung ultramikroskopischer Teilchen, mit besonderer Anwendung auf Goldrubiingläser (German) [Visualization and size measurement of ultramicroscopic particles, with special application to gold-colored ruby glass],” *Ann. d. Phys.* **10**, 1–39 (1903).

- [12] R. Brown, “XXVII. A brief account of microscopical observations made in the months of June, July and August 1827, on the particles contained in the pollen of plants; and on the general existence of active molecules in organic and inorganic bodies,” *Phil. Mag.* **4**, 161–173 (1828).
- [13] A. Einstein, “Über die von der molekularkinetischen Theorie der Wärme gefordert Bewegung von in ruhenden Flüssigkeiten suspendierten Teilchen. (German) [On the molecular-kinetic theory of the movement by heat of particles suspended in liquids at rest],” *Ann. d. Phys.* **322**, 549–560 (1905).
- [14] A. Einstein, “Zur Theorie der *Brownischen* Bewegung. (German) [On the theory of Brownian motion],” *Ann. d. Phys.* **324**, 371–381 (1906).
- [15] P. Langevin, “Sur la Théorie du Mouvement Brownien (French) [On the theory of Brownian motion],” *C. R. Acad. Sci. (Paris)* **146**, 530–533 (1908).
- [16] J. B. Perrin, “Le Mouvement Brownien et la Réalité Moleculaire (French) [Brownian movement and molecular reality],” *Ann. Chimi. Phys. (8me Serie)* **18**, 5–114 (1909).
- [17] H. Schulze, “Schwefelarsen in wässriger Lösung (German) [Sulphide in aqueous solutions],” *J. Prakt. Chem.* **25**, 431–452 (1882).
- [18] W. B. Hardy, “A Preliminary Investigation of the Conditions which Determine the Stability of Irreversible Hydrosols,” *J. Phys. Chem.* **4**, 235–253 (1899).
- [19] H. Helmholtz, “Studien über electrische Grenzschichten (German) [Studies of electric boundary layers],” *Ann. d. Phys.* **243**, 337–382 (1879).
- [20] M. v. Smoluchowski, “Contribution à la théorie de l’endosmose électrique et de quelques phénomènes corrélatifs (French) [Contribution to the theory of electroosmosis and related phenomena],” *Bull. Int. Acad. Sci. Cracovie* **8**, 182–200 (1903).
- [21] G. Gouy, “Sur la constitution de la charge électrique à la surface d’un électrolyte (French) [Constitution of the electric charge at the surface of an electrolyte],” *J. Phys. Radium* **9**, 457–468 (1910).
- [22] D. L. Chapman, “LI. A contribution to the theory of electrocapillarity,” *Phil. Mag.* **25**, 475–481 (1913).
- [23] P. Debye and E. Hückel, “Zur Theorie der Electrolyte. I. Gefrierpunkterniedrigung und verwandte Escheinungen. (German) [The theory of electrolytes. I. Lowering of freezing point and related phenomena],” *Phys. Z.* **24**, 185–206 (1923).

- [24] B. Derjaguin and L. Landau, “Theory of the stability of strongly charged lyophobic sols and of the adhesion of strongly charged particles in solutions of electrolytes,” *Acta Physicochim URSS* **14**, 633 (1941).
- [25] A. Klinkenberg and J. L. van der Minne, *Electrostatics in the Petroleum Industry: The Prevention of Explosion Hazards* (Elsevier: New York, 1958).
- [26] J. L. van der Minne and P. H. J. Hermanie, “Electrophoresis measurements in benzene—correlation with stability. I. Development of method,” *J. Colloid Sci.* **7**, 600–615 (1952).
- [27] J. W. Vanderhoff, J. F. Vitkuske, E. B. Bradford, and T. Alfrey, “Some factors involved in the preparation of uniform particle size latexes,” *J. Poly. Sci.* **20**, 225–234 (1956).
- [28] K. E. J. Barrett, *Dispersion Polymerization in Organic Media* (Wiley, 1975).
- [29] L. Antl, J. W. Goodwin, R. D. Hill, R. H. Ottewill, S. M. Owens, S. Papworth, and J. A. Waters, “The preparation of poly(methyl methacrylate) latices in non-aqueous media,” *Colloids Surf.* **17**, 67–78 (1986).
- [30] D. H. Napper, “Flocculation studies of non-aqueous sterically stabilized dispersions of polymer,” *Trans. Faraday Soc.* **64**, 1701–1711 (1968).
- [31] G. M. Kepler and S. Fraden, “Attractive potential between confined colloids at low ionic strength,” *Phys. Rev. Lett.* **73**, 356–359 (1994).
- [32] J. C. Crocker and D. G. Grier, “Microscopic measurement of the pair interaction potential of charge-stabilized colloid,” *Phys. Rev. Lett.* **73**, 352–355 (1994).
- [33] H. M. Lindsay and P. M. Chaikin, “Elastic properties of colloidal crystals and glasses,” *J. Chem. Phys.* **76**, 3774–3781 (1982).
- [34] E. B. Sirota, H. D. Ou-Yang, S. K. Sinha, P. M. Chaikin, J. D. Axe, and Y. Fujii, “Complete phase diagram of a charged colloidal system: A synchrotron x-ray scattering study,” *Phys. Rev. Lett.* **62**, 1524–1527 (1989).
- [35] Y. Monovoukas and A. P. Gast, “The experimental phase diagram of charged colloidal suspensions,” *J. Colloid Interface Sci.* **128**, 533–548 (1989).
- [36] J. W. Merrill, S. K. Sainis, and E. R. Dufresne, “Many-body electrostatic forces between colloidal particles at vanishing ionic strength,” *Phys. Rev. Lett.* **103**, 138301 (2009).

- [37] J. W. Merrill, S. K. Sainis, J. Blawdziewicz, and E. R. Dufresne, “Many-body force and mobility measurements in colloidal systems,” *Soft Matter* **6**, 2187–2192 (2010).
- [38] A. Ashkin, J. M. Dziedzic, J. E. Bjorkholm, and S. Chu, “Observation of a single-beam gradient force optical trap for dielectric particles,” *Opt. Lett.* **11**, 288–290 (1986).
- [39] D. G. Grier and Y. Roichman, “Holographic optical trapping,” *Appl. Opt.* **45**, 880–887 (2006).
- [40] J. C. Crocker and D. G. Grier, “When like charges attract: The effects of geometrical confinement on long-range colloidal interactions,” *Phys. Rev. Lett.* **77**, 1897–1900 (1996).
- [41] S. K. Sainis, V. Germain, and E. R. Dufresne, “Statistics of particle trajectories at short time intervals reveal fN-scale colloidal forces,” *Phys. Rev. Lett.* **99**, 018303 (2007).
- [42] S. K. Sainis, V. Germain, C. O. Mejean, and E. R. Dufresne, “Electrostatic interactions of colloidal particles in nonpolar solvents: Role of surface chemistry and charge control agents,” *Langmuir* **24**, 1160–1164 (2008).
- [43] S. K. Sainis, J. W. Merrill, and E. R. Dufresne, “Electrostatic interactions of colloidal particles at vanishing ionic strength,” *Langmuir* **24**, 13334–13337 (2008).
- [44] S. Alexander, P. M. Chaikin, P. Grant, G. J. Morales, P. Pincus, and D. Hone, “Charge renormalization, osmotic pressure, and bulk modulus of colloidal crystals: Theory,” *J. Chem. Phys.* **80**, 5776–5781 (1984).
- [45] G. M. Bell, S. Levine, and L. N. McCartney, “Approximate methods of determining the double-layer free energy of interaction between two charged colloidal spheres,” *J. Colloid Interface Sci.* **33**, 335–359 (1970).
- [46] J. C. Crocker, *Probing Colloidal Interactions with Digital Video Microscopy and Blinking Optical Tweezers*, Ph.D. thesis, University of Chicago (1997).
- [47] G. V. Ramanathan, “Counterion condensation in micellar and colloidal solutions,” *The Journal of Chemical Physics* **88**, 3887–3892 (1988).
- [48] E. R. Weeks, J. C. Crocker, A. C. Levitt, A. Schofield, and D. A. Weitz, “Three-dimensional direct imaging of structural relaxation near the colloidal glass transition,” *Science* **287**, 627–631 (2000).

- [49] A. D. Dinsmore, E. R. Weeks, V. Prasad, A. C. Levitt, and D. A. Weitz, “Three-dimensional confocal microscopy of colloids,” *Appl. Opt.* **40**, 4152–4159 (2001).
- [50] E. H. A. de Hoog, *Interfaces and crystallization in colloid-polymer suspensions*, Ph.D. thesis, Utrecht University (2001).
- [51] M. E. Leunissen, *Manipulating Colloids with Charge and Electric Fields*, Ph.D. thesis, Utrecht University (2007).
- [52] C. P. Royall, M. E. Leunissen, and A. van Blaaderen, “A new colloidal model system to study long-range interactions quantitatively in real space,” *J. Phys.: Condens. Matter* **15**, S3581 (2003).
- [53] W. M. Heston, E. J. Hennelly, and C. P. Smyth, “Dielectric constants, viscosities, densities, refractive indices and dipole moment calculations for some organic halides,” *J. Am. Chem. Soc.* **72**, 2071–2075 (1950).
- [54] W. M. Haynes, *CRC Handbook of Chemistry and Physics*, 94th ed., edited by D. R. Lide and T. J. Bruno (CRC Press, Boca Raton, FL, 2013).
- [55] A. I. Vogel, “365. Physical properties and chemical constitution. Part XIX. Five-membered and six-membered carbon rings,” *J. Chem. Soc.* , 1809–1813 (1948).
- [56] D. R. Lide and G. W. A. Milne, *Handbook of Data on Organic Compounds*, Handbook of Data on Organic Compounds, Vol. 4; 7 (CRC Press, Boca Raton, FL, 1994).
- [57] J. A. Riddick, W. B. Bunger, and T. K. Sakano, *Organic Solvents: Physical Properties and Methods of Purification*, 4th ed., edited by A. Weissberger, Techniques of Chemistry, Vol. 2 (Wiley, New York, 1986).
- [58] M. E. Leunissen, A. van Blaaderen, A. D. Hollingsworth, M. T. Sullivan, and P. M. Chaikin, “Electrostatics at the oil-water interface, stability, and order in emulsions and colloids,” *PNAS* **104**, 2585–2590 (2007).
- [59] M. E. Leunissen, J. Zwanikken, R. van Roij, P. M. Chaikin, and A. van Blaaderen, “Ion partitioning at the oil-water interface as a source of tunable electrostatic effects in emulsions with colloids,” *Phys. Chem. Chem. Phys.* **9**, 6405–6414 (2007).
- [60] C. Valeriani, P. J. Camp, J. W. Zwanikken, R. van Roij, and M. Dijkstra, “Ion association in low-polarity solvents: comparisons between theory, simulation, and experiment,” *Soft Matter* **6**, 2793–2800 (2010).
- [61] A. B. Pangborn, M. A. Giardello, R. H. Grubbs, R. K. Rosen, and F. J. Timmers, “Safe and convenient procedure for solvent purification,” *Organometallics* **15**, 1518–1520 (1996).

- [62] J. G. Smith, in *Organic Chemistry* (McGraw-Hill, New York, 2011) 3rd ed., Chap. 8: Alkyl halides and elimination reactions.
- [63] R. G. Schmitt, *The Kinetics of the Hydrolysis of Bromocyclohexane*, Master's thesis, Worcester Polytechnic Institute (1953).
- [64] G. J. Janz and S. S. Danyluk, "Hydrogen Halides in Acetonitrile. III. Electrical Conductance," *J. Am. Chem. Soc.* **81**, 3854–3858 (1959).
- [65] M. N. Sovilj, "Kinematic viscosities of binary and ternary liquid mixtures involving chloroform, 2-propanol, and 2-butanol at several temperatures," *J. Chem. Eng. Data* **40**, 1058–1061 (1995).
- [66] R. K. Shukla, A. Kumar, N. Awasthi, U. Srivastava, and V. S. Gangwar, "Density, viscosity and refractive index of binary liquid mixtures at 293.15, 298.15, 303.15, 308.15 and 313.15 K," *Exp. Therm. and Fluid Sci.* **37**, 1–11 (2012).
- [67] H. Looyenga, "Dielectric constants of homogeneous mixture," *Mol. Phys.* **9**, 501–511 (1965).
- [68] S. Prakash, J. D. Pandey, and R. Singh, "Kinetics and mechanism of sonochemical decomposition of aqueous bromoform solution," *J. Prakt. Chem.* **26**, 140–146 (1964).
- [69] G. Bosma, C. Pathmamanoharan, E. H. A. de Hoog, W. K. Kegel, A. van Blaaderen, and H. N. W. Lekkerkerker, "Preparation of monodisperse, fluorescent PMMA–latex colloids by dispersion polymerization," *J. Colloid Interface Sci.* **245**, 292–300 (2002).
- [70] M. T. Elsesser and A. D. Hollingsworth, "Revisiting the synthesis of a well-known comb-graft copolymer stabilizer and its application to the dispersion polymerization of poly(methyl methacrylate) in organic media," *Langmuir* **26**, 17989–17996 (2010).
- [71] W. K. Kegel and A. van Blaaderen, "Direct observation of dynamical heterogeneities in colloidal hard-sphere suspensions," *Science* **287**, 290–293 (2000).
- [72] S. Auer, W. C. K. Poon, and D. Frenkel, "Phase behavior and crystallization kinetics of poly-12-hydroxystearic-coated polymethylmethacrylate colloids," *Phys. Rev. E* **67**, 020401 (2003).
- [73] S. H. Behrens and D. G. Grier, "The charge of glass and silica surfaces," *J. Chem. Phys.* **115**, 6716–6721 (2001).

- [74] R. H. Ottewill, A. R. Rennie, and A. Schofield, “The effect of electric fields on nonaqueous dispersions,” in *Trends in Colloid and Interface Science IV*, Progress in Colloid & Polymer Science, Vol. 81, edited by M. Zulauf, P. Lindner, and P. Terech (Steinkopff, Darmstadt, 1990) pp. 1–5.
- [75] C. F. Zukoski, A. P. Gast, D. A. Saville, S. P. Stoylov, B. Vincent, J. Lyklema, P. C. van der Hoeven, P. Bartlett, R. H. Ottewill, A. Schofield, G. Frens, G. Cevel, R. Buscall, N. Ise, M. H. G. M. Penders, J. K. G. Dhont, A. Vrij, W. B. Russel, T. F. Tadors, A. E. Duisterwinkel, and H. J. Ploehm, “General discussion,” *Faraday Discuss. Chem. Soc.* **90**, 57–75 (1990).
- [76] M. N. van der Linden, J. C. P. Stiefelhagen, G. Heessels-Gürboğa, J. E. S. van der Hoeven, N. A. Elbers, M. Dijkstra, and A. van Blaaderen, “Charging of Poly(methyl methacrylate) (PMMA) Colloids in Cyclohexyl Bromide: Locking, Size Dependence, and Particle Mixtures,” *Langmuir* **31**, 65–75 (2015).
- [77] C. P. Smyth, *Dielectric Behavior and Structure* (McGraw-Hill, New York, 1955).
- [78] J. Israelachvili, *Intermolecular and Surface Forces* (Elsevier, London, 1992).
- [79] J. A. Weiss, A. E. Larsen, and D. G. Grier, “Interactions, dynamics, and elasticity in charge-stabilized colloidal crystals,” *J. Chem. Phys.* **109**, 8659–8666 (1998).
- [80] E. R. Dufresne, G. C. Spalding, M. T. Dearing, S. A. Sheets, and D. G. Grier, “Computer-generated holographic optical tweezer arrays,” *Rev. Sci. Instrum.* **72**, 1810–1816 (2001).
- [81] A. Ashkin, “Forces of a single-beam gradient laser trap on a dielectric sphere in the ray optics regime,” in *Methods in Cell Biology*, Vol. 55, edited by M. P. Sheetz (Academic Press, 1998) pp. 1–27.
- [82] D. G. Grier, “A revolution in optical manipulation,” *Nature* **424**, 810–816 (2003).
- [83] B. T. Draine and J. Goodman, “Beyond Clausius-Mossotti: Wave propagation on a polarizable point lattice and the discrete dipole approximation,” *Astrophys. J.* **405**, 685–697 (1993).
- [84] P. C. Chaumet and M. Nieto-Vesperinas, “Time-averaged total force on a dipolar sphere in an electromagnetic field,” *Opt. Lett.* **25**, 1065–1067 (2000).
- [85] J. P. Gordon, “Radiation forces and momenta in dielectric media,” *Phys. Rev. A* **8**, 14–21 (1973).
- [86] D. B. Ruffner and D. G. Grier, “Comment on ‘Scattering forces from the curl of the spin angular momentum of a light field’,” *Phys. Rev. Lett.* **111**, 059301 (2013).

- [87] Y. Roichman, B. Sun, Y. Roichman, J. Amato-Grill, and D. G. Grier, “Optical forces arising from phase gradients,” *Phys. Rev. Lett.* **100**, 013602 (2008).
- [88] E. R. Dufresne and D. G. Grier, “Optical tweezer arrays and optical substrates created with diffractive optics,” *Rev. Sci. Instrum.* **69**, 1974–1977 (1998).
- [89] S.-H. Lee, *Brownian Motion in Complex Potential Energy Landscapes Created with Light*, Ph.D. thesis, New York University (2007).
- [90] J. W. Goodman, *Introduction to Fourier Optics*, 3rd ed. (Roberts & Company, 2005).
- [91] F. Li, N. Mukohzaka, N. Yoshida, Y. Igasaki, H. Toyoda, T. Inoue, Y. Kobayashi, and T. Hara, “Phase modulation characteristics analysis of optically-addressed parallel-aligned nematic liquid crystal phase-only spatial light modulator combined with a liquid crystal display,” *Opt. Rev.* **5**, 174–178 (1998).
- [92] G. D. Love, “Wave-front correction and production of zernike modes with a liquid-crystal spatial light modulator,” *Appl. Opt.* **36**, 1517–1524 (1997).
- [93] J. E. Curtis and D. G. Grier, “Structure of optical vortices,” *Phys. Rev. Lett.* **90**, 133901 (2003).
- [94] Y. Roichman and D. G. Grier, “Three-dimensional holographic ring traps,” *Proc. SPIE* **6483**, 64830F–1–5 (2007).
- [95] S.-H. Lee, Y. Roichman, and D. G. Grier, “Optical solenoid beams,” *Opt. Express* **18**, 6988–6993 (2010).
- [96] D. B. Ruffner and D. G. Grier, “Optical conveyors: A class of active tractor beams,” *Phys. Rev. Lett.* **109**, 163903 (2012).
- [97] T. Savin and P. S. Doyle, “Static and dynamic errors in particle tracking microrheology,” *Biophys. J.* **88**, 623–638 (2005).
- [98] J. C. Crocker and D. G. Grier, “Methods of digital video microscopy for colloidal studies,” *J. Colloid Interface Sci.* **179**, 298–310 (1996).
- [99] S.-H. Lee, Y. Roichman, G.-R. Yi, S.-H. Kim, S.-M. Yang, A. van Blaaderen, P. van Oostrum, and D. G. Grier, “Characterizing and tracking single colloidal particles with video holographic microscopy,” *Opt. Express* **15**, 18275–18282 (2007).
- [100] C. Hollitt, “A convolution approach to the circle Hough transform for arbitrary radius,” *Mach. Vision Appl.* **24**, 683–694 (2013).

- [101] D. H. Ballard, “Generalizing the Hough transform to detect arbitrary shapes,” *Pattern Recogn.* **13**, 111–122 (1981).
- [102] B. J. Krishnatreya and D. G. Grier, “Fast feature identification for holographic tracking: the orientation alignment transform,” *Opt. Express* **22**, 12773–12778 (2014).
- [103] A. Savitzky and M. J. E. Golay, “Smoothing and differentiation of data by simplified least squares procedures.” *Anal. Chem.* **36**, 1627–1639 (1964).
- [104] B. J. Krishnatreya, A. Colen-Landy, P. Hasebe, B. A. Bell, J. R. Jones, A. Sundar-Meya, and D. G. Grier, “Measuring Boltzmann’s constant through holographic video microscopy of a single colloidal sphere,” *Am. J. Phys.* **82**, 23–31 (2014).
- [105] C. Pozrikidis, *Boundary integral and singularity methods for linearized viscous flow* (Cambridge University Press, Cambridge, UK, 1992).
- [106] D. G. Grier and S. H. Behrens, “Interactions in colloidal suspensions,” in *Electrostatic Effects in Soft Matter and Biophysics*, NATO Science Series, Vol. 46, edited by C. Holm, P. Kékicheff, and R. Podgornik (Springer Netherlands, 2001) pp. 87–116.
- [107] G. K. Batchelor, “Brownian diffusion of particles with hydrodynamic interaction,” *J. Fluid Mech.* **74**, 1–29 (1976).
- [108] B. Silverman, *Density Estimation for Statistics and Data Analysis* (Chapman & Hall/CRC, 1998).
- [109] V. A. Epanechnikov, “Non-parametric estimation of a multivariate probability density,” *Theory Probab. Appl.* **14**, 153–158 (1969).
- [110] T. Savin and P. S. Doyle, “Role of a finite exposure time on measuring an elastic modulus using microrheology,” *Phys. Rev. E* **71**, 041106 (2005).
- [111] E. Trizac, L. Bocquet, and M. Aubouy, “Simple approach for charge renormalization in highly charged macroions,” *Phys. Rev. Lett.* **89**, 248301 (2002).
- [112] E. Trizac, L. Bocquet, M. Aubouy, and H. H. von Grünberg, “Alexander’s prescription for colloidal charge renormalization,” *Langmuir* **19**, 4027–4033 (2003).
- [113] T. Vissers, A. Imhof, F. Carrique, A. V. Delgado, and A. van Blaaderen, “Electrophoresis of concentrated colloidal dispersions in low-polar solvents,” *J. Colloid Interface Sci.* **361**, 443–455 (2011).

- [114] D. A. J. Gillespie, J. E. Hallett, O. Elujoba, A. F. Che Hamzah, R. M. Richardson, and P. Bartlett, “Counterion condensation on spheres in the salt-free limit,” *Soft Matter* **10**, 566–577 (2014).
- [115] R. Tuinier, “Approximate solutions to the Poisson-Boltzmann equation in spherical and cylindrical geometry,” *J. Colloid Interface Sci.* **258**, 45–49 (2003).